Molecular Therapy
Original Article

M2 macrophages secrete glutamate-containing extracellular vesicles to alleviate osteoporosis by reshaping osteoclast precursor fate

Xiaoyuan Huang,[1,3] Yanhua Lan,[1,3] Jiahui Shen,[1,3] Xiaomin Zhao,[2] Yanyan Zhou,[1] Wenzhi Wu,[1] Jiajie Mao,[1] Yuzhu Wu,[1] Zhijian Xie,[1] and Zhuo Chen[1]

[1]Stomatology Hospital, School of Stomatology, Zhejiang University School of Medicine, Zhejiang Provincial Clinical Research Center for Oral Diseases, Key Laboratory of Oral Biomedical Research of Zhejiang Province, Cancer Center of Zhejiang University, Engineering Research Center of Oral Biomaterials and Devices of Zhejiang Province, Hangzhou 310006, China; [2]Department of Stomatology, Shanghai Pudong Hospital, Fudan University Pudong Medical Center, 2800 Gongwei Road, Pudong, Shanghai 201399, China

Osteoclast precursors (OCPs) are thought to commit to osteoclast differentiation, which is accelerated by aging-related chronic inflammation, thereby leading to osteoporosis. However, whether the fate of OCPs can be reshaped to transition into other cell lineages is unknown. Here, we showed that M2 macrophage-derived extracellular vesicles (M2-EVs) could reprogram OCPs to downregulate osteoclast-specific gene expression and convert OCPs to M2 macrophage-like lineage cells, which reshaped the fate of OCPs by delivering the molecular metabolite glutamate. Upon delivery of glutamate, glutamine metabolism in OCPs was markedly enhanced, resulting in the increased production of α-ketoglutarate (αKG), which participates in Jmjd3-dependent epigenetic reprogramming, causing M2-like macrophage differentiation. Thus, we revealed a novel transformation of OCPs into M2-like macrophages via M2-EVs-initiated metabolic reprogramming and epigenetic modification. Our findings suggest that M2-EVs can reestablish the balance between osteoclasts and M2 macrophages, alleviate the symptoms of bone loss, and constitute a new approach for bone-targeted therapy to treat osteoporosis.

INTRODUCTION

Chronic, low-grade, sterile inflammation is almost universally associated with aging.[1] Chronic inflammation in older individuals increases the secretion of proinflammatory cytokines, chemokines, and other molecules from cells.[2] Aging-related chronic inflammation leads to osteoclast (OC) overdifferentiation and hyperfunction, and bone remodeling is interrupted in favor of bone resorption, which causes bone loss and predisposes the skeleton to fractures.[3] Osteoporosis reflects an imbalance in the activities of osteoblasts (OBs) and OCs that leads to decreased bone mass and integrity[4,5]; therefore, interfering with OC maturation is a vital way to prevent OC-associated osteoporosis.

Mature OCs are multinuclear macrophage -like cells derived from hematopoietic stem cells. Macrophage colony-stimulating factor (M-CSF) and receptor activator of nuclear factor-κB ligand (RANKL) induce OCPs to express genes related to OC lineage allocation and maturation.[6] OCPs are committed to differentiating into OCs in the bone microenvironment; however, whether OCPs can differentiate into other lineages is unclear. Reprogramming OCP maturation during this critical period of cell differentiation would be therapeutically valuable. It is well known that macrophages are derived from monocytes and differentiate into M1 or M2 macrophages in response to different stimuli.[7] Exposure to interferon-γ and lipopolysaccharide drives M1 macrophages to secrete potentiated cytotoxic and antitumoral factors. In contrast, M2 macrophages, which tend to support immunoregulation and tissue regeneration, are promoted by stimulation with interleukin-4 (IL-4), IL-13, or IL-10.[8] Interconversion between M1 macrophages and M2 macrophages has been widely confirmed, and controlling the macrophage phenotypic switch from M1 to M2 at specific time points is a promising way to control the transition from the inflammatory phase to the proliferation phase of the repair and remodeling process.[9–11] Whether OCPs, which are also monocyte lineage-derived cells, can be specifically transformed into M2 macrophages remains unclear.

Received 18 July 2023; accepted 2 February 2024;
https://doi.org/10.1016/j.ymthe.2024.02.005.

[3]These authors contributed equally

Correspondence: Zhijian Xie, Stomatology Hospital, School of Stomatology, Zhejiang University School of Medicine, Zhejiang Provincial Clinical Research Center for Oral Diseases, Key Laboratory of Oral Biomedical Research of Zhejiang Province, Cancer Center of Zhejiang University, Engineering Research Center of Oral Biomaterials and Devices of Zhejiang Province, Hangzhou 310006, China.
E-mail: xzj66@zju.edu.cn
Correspondence: Zhuo Chen, Stomatology Hospital, School of Stomatology, Zhejiang University School of Medicine, Zhejiang Provincial Clinical Research Center for Oral Diseases, Key Laboratory of Oral Biomedical Research of Zhejiang Province, Cancer Center of Zhejiang University, Engineering Research Center of Oral Biomaterials and Devices of Zhejiang Province, Hangzhou 310006, China.
E-mail: zoechen@zju.edu.cn

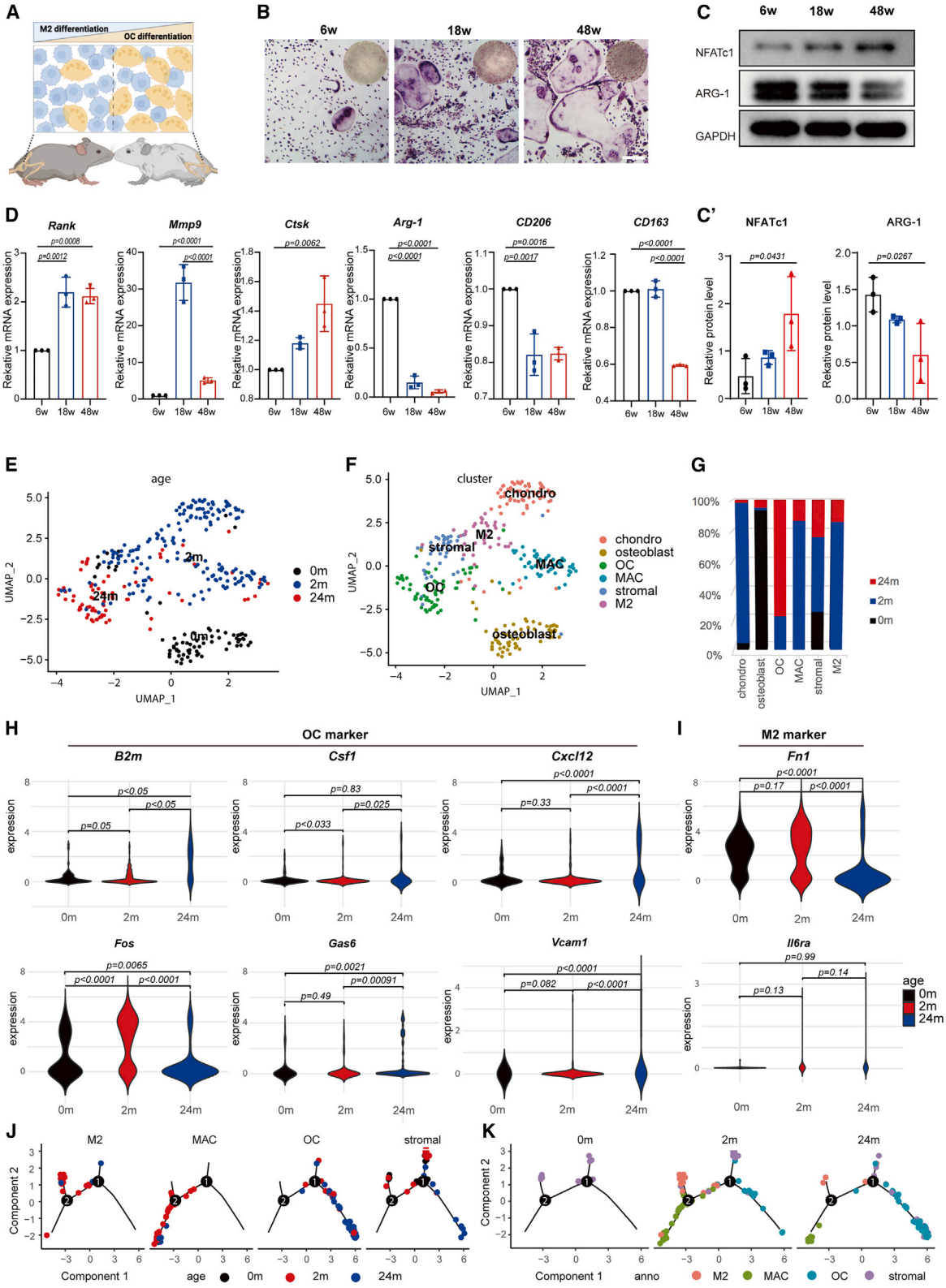

(legend on next page)

We predict that extracellular vesicles (EVs) could act as "gene editors" in this cell transformation process. EVs are small vesicular nanoparticles secreted by various cells and are key mediators of intercellular communication. Like parent cells or other same-lineage cells, EVs exhibit receptor-ligand binding. Therefore, EVs can function as effective vectors for targeted cell delivery. Specifically, EVs can carry and deliver particular compositions of proteins, lipids, RNAs, DNAs, and small molecules (metabolites) to recipient cells.[12] Upon release of their contents, EVs can effectively guide phenotypic switching to directly reprogram resident M1 macrophages into M2 macrophages or reprogram multipotential stem cells.[13] Previously, we demonstrated that EVs are key participants in the progression of bone remodeling progression.[14,15]Therefore, in the present study, we investigated the role of EVs in macrophage transformation.

Here, we found that EVs isolated from alternatively activated M2 macrophages (M2-EVs), through the release of specific metabolites, could induce direct reprogramming of OCPs into M2-like macrophages to maintain balance. The reprogrammed M2-like macrophages exhibited an inhibited OC phenotype and function and became committed to the M2 macrophage lineage.[16] Multiomics analysis revealed that glutamine metabolism and the expression of lysine-specific demethylases (Jumonji domain-containing histone demethylases [Jmjds]) were significantly enhanced. Jumonji domain containing-3 (Jmjd3), a histone 3 Lys27 (H3K27) demethylase, is a key enzyme for the demethylation of H3K27 and has been implicated in the activation of M2 macrophages.[17] Therefore, we hypothesized that M2-EVs regulate glutamine metabolism in OCPs and increase the α-ketoglutarate (αKG) content and nuclear intake, assisting in the activation of Jmjds. After characterizing the biophysical and biochemical properties of M2-EVs, we applied M2-EVs to osteoporotic mice to drive *in situ* EV-guided macrophage phenotypic switching. These findings extend our understanding of the interconversions of macrophage-like cells and suggest a novel strategy that guides the transformation of bone-damaging cells into bone-repairing cells via EVs.

RESULTS

Aging affects the bone marrow-derived macrophage (BMM) function in the BM niche

To elucidate the ability of BMMs to differentiate into OCs or M2 macrophages at different ages, BMMs were isolated from mouse femurs and tibias from 6-, 18-, and 48-week-olds. BMMs were treated with M-CSF and RANKL or IL-4 to induce M2 or OC differentiation (Figure 1A). A positive correlation was found between OC differentiation and senescence. The tartrate-resistant acid phosphatase (TRAP) staining revealed an age-related increase in OC differentiation (Figure 1B). Western blot analysis revealed that the level of an OC-specific protein (NFATc1) increased from the 6-week-old to the 18-week-old, whereas the level of an M2-specific protein (ARG-1) also decreased (Figure 1C). Quantitative real-time PCR revealed that senescence increased the expression of OC markers (Rank, Mmp9, and Ctsk) and suppressed the expression of M2 markers (Arg-1, CD206, and CD163) (Figure 1D).

Furthermore, replication analysis was performed via the same procedure using a published single-cell analysis dataset (GEO: GSE161946). Using Leiden clustering on quality-filtered cells, we identified three age subpopulations and six cluster subpopulations with transcriptomic profiles that differed in subtle ways. Based on known cell-type marker genes (Table S1), these clusters were subsequently annotated as "chondro," "osteoblast," "OC," "MAC," "stromal," and "M2" cell populations encompassing three ages: 0 months, 2 months, and 24 months (Figures 1E and 1F). The 24-month-old mice cell were most abundant in the OC cluster and least abundant in the M2 macrophage cluster, in contrast to those from 0- and 2-month-old mice.[1] These findings corresponded to the observations that senescence reduced M2 macrophage differentiation and enhanced OC formation (Figure 1G). The data from single cells showing OC and M2 macrophage-related gene expression are shown in violin plots and grouped by age (Figures 1H and 1I). The results clearly indicated that the expression of OC markers (B2m, Csf1, Cxcl12, Fos, Gas6, and Vcam1) was increased, whereas that of M2 markers (Fn1 and Il6ra) was decreased. Next, four clusters with progenitor properties—M2, MAC, OC, and stromal clusters—were identified and used to construct a new trajectory from MAC. M2 and OC cell branches were revealed from the trajectory tree; 0- and 2-month-old cells tended to aggregate at the M2 branches of the tree, whereas 24-month-old cells accumulated at the OC branches of the tree (Figures 1J and 1K).

EV-guided reprogramming of OCPs into M2 macrophages *in vitro*

To investigate what caused the difference in BMM differentiation, a NanoFCM assay was performed. The results were that senescence suppressed macrophage-derived exosome secretion, which was positive for CD206 and CD163, revealing that senescence results in fewer M2 macrophages EVs (Figure 2A). Notably, consistent with OC differentiation,[6,18] multinucleated cells were not predominant before 3 days, when the majority of sites were occupied by mononucleated cells.

Figure 1. Age-related alterations in BMM differentiation

(A) Schematic representation of cell differentiation. (B) Representative TRAP images showing that BMMs differentiated into OCs from 6-week-old (6w), 18-week-old (18w) and 48-week-old (48w) mice. Scale bar, 200 μm. (C) Western blot analysis (C) and qualification (C′) of ARG-1 and NFATc1. (D) Quantitative real-time PCR analyses of OC and M2 macrophage gene markers (n = 3). (E and F) Heatmap of the top 150 differentially expressed genesDEGs in each age group according to Leiden clustering. Uniform manifold approximation and projection (UMAP) plot showing Leiden clusters from combined Smart-seq2 scRNA-seq data of single cells from chondro, M2, stromal, OC, MAC and osteoblast clusters (E) and from postnatal day 3, 0-, 2-, and 24-month-old mice (F). (G) Clustering of the same UMAP plot by age (top), showing the distribution within Leiden clusters (bottom) of sequenced single cells by age. (H and I) Single-cell data for selected OC (H) or M2 macrophage-associated genes (I) are shown as violin plots grouped by age. (J and K) The cells are colored according to the time when the SSCs were extracted according to the cell cluster (left) and age (right). One-way ANOVA with Tukey's (C′ and D) or Kruskal-Wallis multiple comparisons test (H and I).

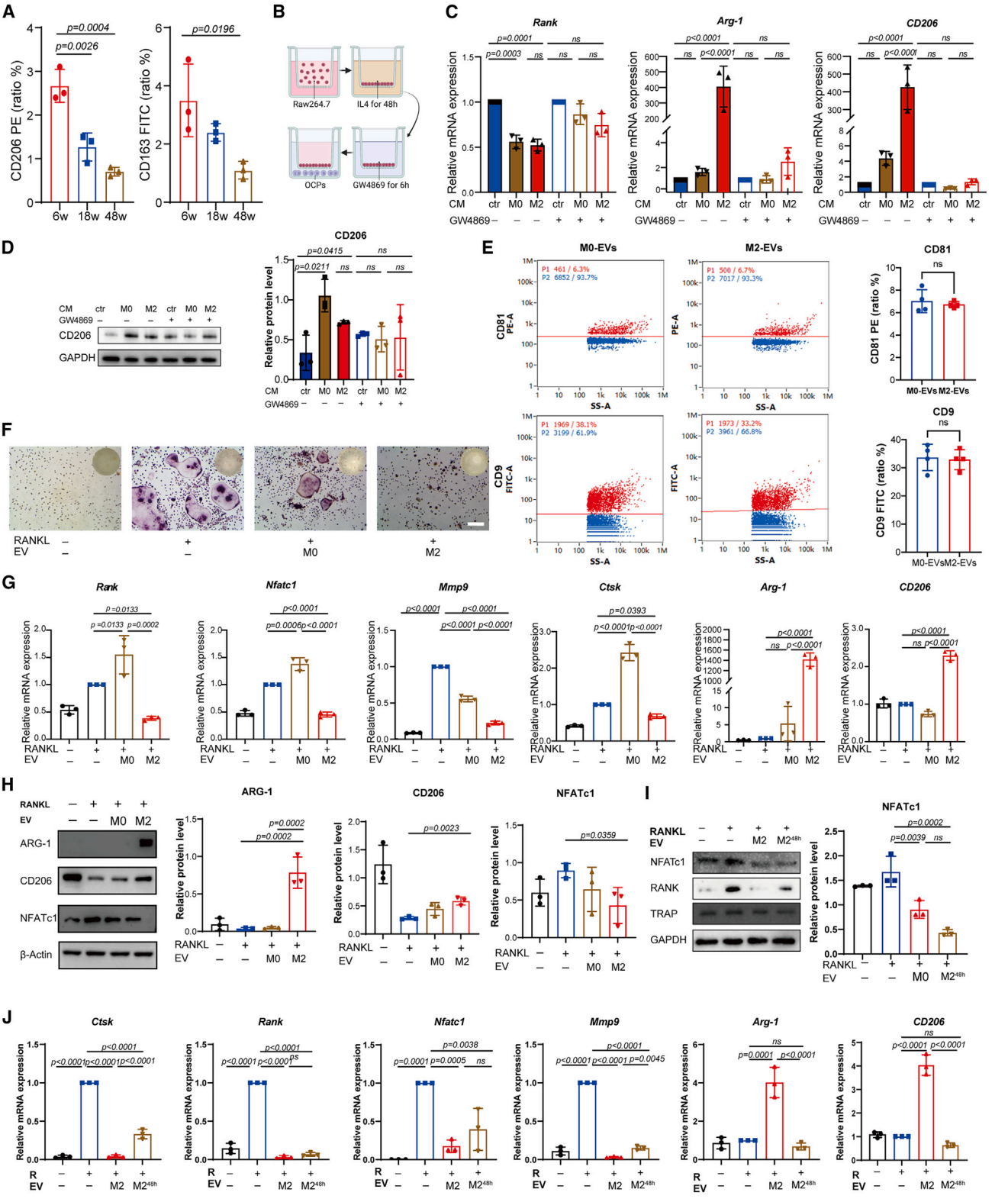

(legend on next page)

The expression of genes that typify the OC lineage, including Rank, Ctsk, and Mmp9, was not significantly different between OCs at 3 days (immature OCs) and OCs at 5 days (mature OCs) (Figures S1A and S1B). These findings suggest that OCPs are important regulatory nodal points during OC differentiation. OCP cultures were cultured with conditioned medium (CM) collected from M0 and M2 macrophages (M0-CM and M2-CM) for 2 days. Surprisingly, the mRNA expression of Rank, an OC marker, decreased, and the mRNA expression of M2 macrophage markers, including Arg-1 and CD206 as well as the protein level of CD206, substantially increased. However, these changes in the gene expression of OCPs were strongly impaired when EV production was inhibited by treatment with GW4869, an inhibitor of EV biogenesis and release (Figures 2B–2D). These results suggest that the ability of M2-CM to change differentiation is at least partly dependent on M2-EVs.[19] EVs are endosome-derived vesicles that mediate cell-to-cell communication. M0 and M2 macrophage culture media were ultracentrifuged to harvest EVs. The viability of the donor cells was greater than 98% (Figures S2A). Flow cytometric analysis did not reveal any significant difference in the live/dead ratio of macrophages following IL-4 treatment (Figure S2B). Upon exposure to IL-4, RAW264.7 cells were successfully induced to polarize to the M2 phenotype, as evidenced by flow cytometric analysis, which revealed that the percentage of $CD206^+$ cells exceeded 50% after IL-4 treatment (Figure S2C). We first tested the purity of our EV isolation approach via electron microscopy, nanoparticle tracking analysis (NTA), Western blot assays, and NanoFCM according to the 2022 guidelines of the International Society for Extracellular Vesicles. As expected, the EVs expressed positive EV markers, such as Alix, Flotillin-1, Annexin V, CD9, CD54, EpCAM, and they were negative for the EV marker Calnexin and GM130. Transmission electron microscopy (TEM) and NTA demonstrated that the size of the isolated EVs was 100–200 nm, in accordance with EV identification standards (Figures S3A–S3C). The NanoFCM result showed that most of the particles in M0-EVs or M2-EVs were distributed between 55 and 100 nm in size. After being treated with 1% Triton X-100, M0-EVs yielded the highest recovery rate, 68.2%, and M2-EVs yielded a recovery rate of 76.8% (Figure S3D). The percentages of $CD9^+$ EVs ranged between 6.3% and 6.8%, and the percentage of $CD81^+$ EVs ranged between 33.2% and 38.1% (Figure 2E). To further examine the ability of EVs to regulate OCP fate, we constructed an EV-guided coculture system. Moreover, significantly more donor-derived $TRAP^+$ osteoclastic areas were observed on day 7 callus sites after M0-EV treatment than after M2-EVs treatment (Figure 2F). M2-EVs obviously decreased the mRNA expression of OC markers (Rank, Nfatc1, Mmp9, and Ctsk) and increased the expression of M2 markers (Arg-1 and CD206) (Figures 2G). The protein levels of ARG-1 and CD206 were upregulated against the downregulation of NFATc1 (Figure 2H). However, the downregulation of relative mRNA expression of Rank by M0-CM is inconsistent with M0-EVs, which may be attributed to the presence of other active components in the CM, including maternal leukocytes, growth factors, and cytokines, excluding EVs.[20] In comparison to M2-EVs, EVs derived from M2 macrophages following a 48-h induction with IL-4 did not demonstrate superior proficiency in the phenotypic characteristics of OCPs, nor did the macrophages that secreted these EVs exhibit enhanced cell viability (Figures 2I, 2J, and S2D). Therefore, it is plausible that the EVs selected within the initial 48-h period may possess superior capabilities. Confocal fluorescence microscopy revealed that OCP endocytosis by M2-EVs peaked at 6 h after coculture with EVs (Figure S3E). Since EVs are known to participate in the exchange of some phenotypic traits between cells,[21] the level of ARG-1 in EVs was also analyzed to exclude the possibility of simple transfer of M2-specific marker proteins from donor to recipient cells via EVs. M2-EVs did not contain the M2-specific protein ARG-1 (Figure S3A). These results suggested that OCPs regulate the transcription of the Arg-1 and CD206 genes after treatment with M2-EVs. In contrast, supplementation with M0-EVs did not significantly influence or even reverse the transformation of OCPs. The above results suggest that OCPs initiate the reprogramming process upon treatment with M2-EVs.

M2-EVs induce a switch in OCPs to an M2 macrophage-like phenotype

Given the observed direct effect and uptake of M2-EVs, M2-EVs labeled with a lipophilic dye (PKH67) were injected into the target cells. Interestingly, more PKH67-labeled M2-EVs than BM stromal cells (BMSCs) were taken up by BMMs, which showed that BMMs had a better ability to target M2-EVs (Figure 3A and Video S1). These results also demonstrated that M2-EVs were preferentially taken up by their parental cell lineage compared to other types of cells. Next, we treated cells with M2-EVs (100 μM) for 2, 3, 4, or 5 days of RANKL-mediated OC and cultured them for 9 days in total (Figure 3B). The results confirmed that the suppression of OC differentiation gradually weakened over time and that early time points, especially 2 days, may be defining times for the suppression of OC differentiation. (Figures 3C, 3D, and S4A).

Here, we demonstrated that cells incubated with RANKL for 2 days had become OCPs.[22] To investigate whether M2-EVs regulate the

Figure 2. EVs reshape the fate of OCPs

(A) NanoFCM analysis for $CD206^+$ EVs and CD163 EVs from 6-, 18-, and 48-week-old mice (n = 3). (B) Schematic diagram of the CM. (C) Relative mRNA expression levels of Rank, Arg-1, and CD206 in cells cocultured with M0 macrophage or M2 macrophage CM and treated with or without GW4869 (n = 3). (D) Relative protein levels of CD206 in cells cocultured with M0 macrophage or M2 macrophage CM and treated with or without GW4869 (*n* = 3). (E) NanoFCM analysis for CD81 or CD9 from M0-EVs and M2-EVs (n = 3). (F) The proportion of $TRAP^+$ cells was determined in BMMs treated with or without RANKL and/or M0-EVs or M2-EVs. Scale bar, 200 μm. (G) Quantitative real-time PCR was performed to analyze Rank, Nfatc1, Mmp9, Ctsk, Arg-1, and CD206 mRNA expression levels under various culture conditions (n = 3). (H) Representative immunoblots showing the expression of NFATc1 (OC-specific marker), ARG-1 and CD206 (M2 macrophage marker) under the above culture conditions. (I) Western blot was performed to analyze NFATc1, RANK, and TRAP protein levels in M2-EVs and $M2\text{-}EVs^{48h}$. (J) Quantitative real-time PCR was performed to analyze Rank, Nfatc1, Mmp9, Ctsk, Arg-1, and CD206 mRNA expression levels in M2-EVs and $M2\text{-}EVs^{48h}$. One-way ANOVA with Tukey's multiple comparisons test (A, C–E, and G–J).

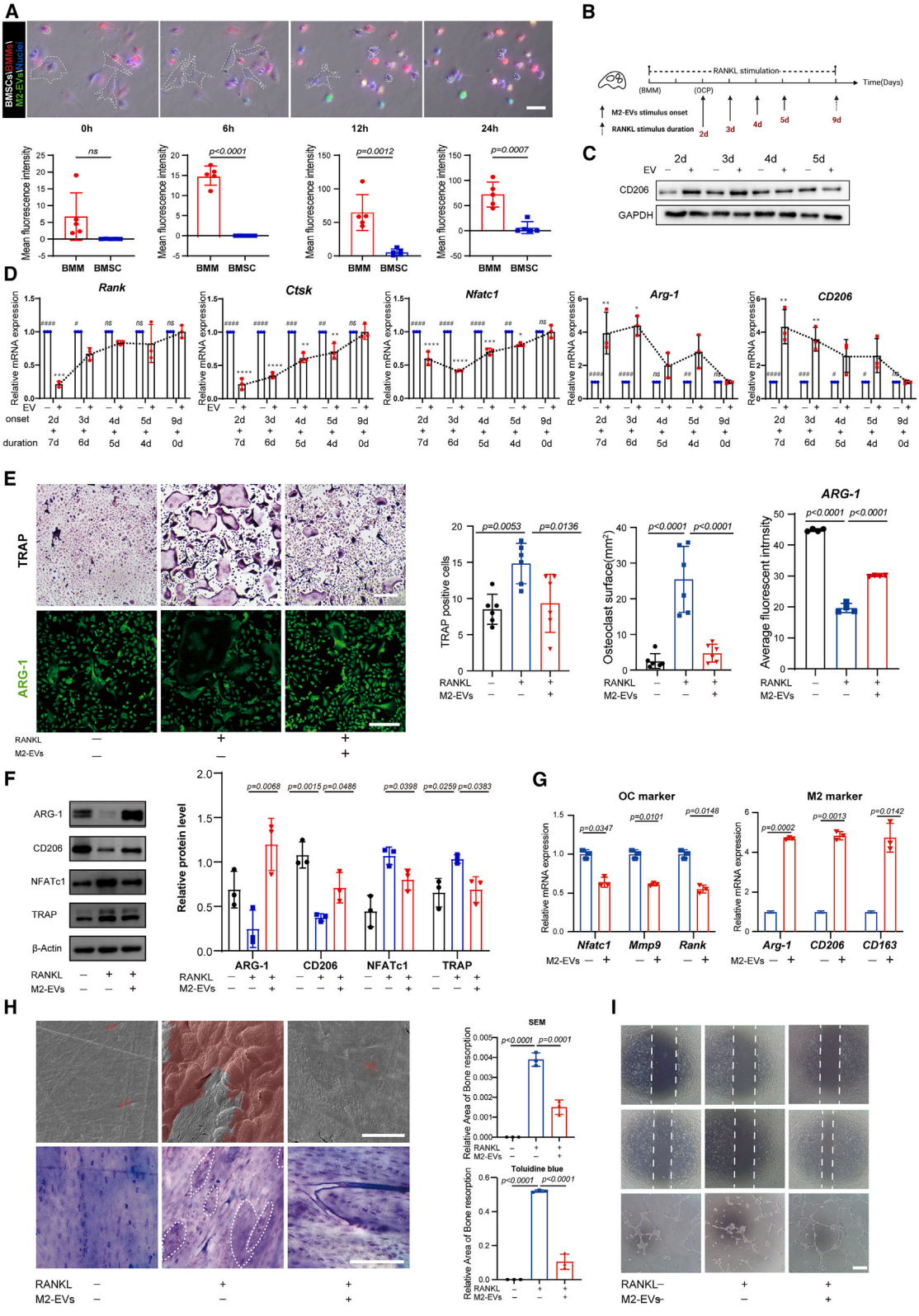

(legend on next page)

differentiation of OCs, BMMs were cultured in the presence of M-CSF and RANKL for 2 days to form OCPs, which were subsequently cocultured with M2-EVs. When the dose was increased from 10 to 100 μg/mL, the live/dead analysis showed that there was no significant difference in cell viability between the different doses of M2-EVs (Figure S4B). Moreover, the cells were continuously cultured for 4 days with or without M2-EVs. Notably, we observed that M2-EVs significantly inhibited the differentiation of OCs in a dose-dependent manner,[23] and almost no giant OCs were observed when the M2-EVs concentration reached 100 μg/mL (Figures S4C–S4E).

Therefore, the optimal M2-EVs stimulation concentration and duration were determined with reference to the OC and M2 macrophage-specific gene expression levels in OCPs. TRAP and immunofluorescence staining revealed that OCPs treated with M2-EVs exhibited less TRAP staining compared to those not treated with M2-EVs (Figure 3E). We also observed that the protein levels of NFATc1 and TRAP were significantly suppressed by M2-EVs treatment. In contrast, the protein levels of the M2 markers ARG-1 and CD206 were upregulated (Figure 3F). The results of the molecular evaluation of OC and M2 markers via quantitative real-time PCR were consistent with the histological data (Figure 3G). Given the influence of M2-EVs on OC differentiation, we next assessed bone resorption ability *in vitro*. OCs cultured on bone slices markedly inhibited the bone resorption pit area after M2-EVs treatment (Figure 3H). *In vitro*, M2-EVs notably augmented the migratory and tube-forming abilities of endothelial cells, with a greater effect observed in M2 macrophages (Figure 3I).

Overall, we demonstrated that inducing OC differentiation during the OCP stage via M2-EVs intervention could transform the cells into the M2-macrophage-like cell lineage. However, M2-EVs inhibited OC differentiation when applied only during the first 3 days in culture, suggesting that the metabolites within these cells target cells in an early osteoclastogenesis stage.

M2-EVs can alleviate osteoporosis

We next investigated whether M2-EVs are capable of attenuating bone loss in adult female C57BL/6 mice. The mice were treated with PBS or M2-EVs and then sacrificed at 8 weeks postsurgery (Figure 4A). Before the formal experiment, the *in vivo* distribution of M2-EVs was compared with that of BMSC-EVs after intravenous administration into the tail vein. The *in vivo* tracing results demonstrated that M2-EVs presented better natural tropism for bone than BMSC-EVs (Figure 4B). There were no histomorphometric differences in the heart, liver, lungs, kidneys, or spleen (Figure S5). In addition, body weight was recorded every week throughout the study. The results demonstrated that M2-EVs protected against bone loss-induced obesity and reduced the mouse body weight to levels closer to those in the sham operation group (Figures 4C and 4D). Femur bones were collected for microcomputed tomography (micro-CT) analysis (Figure 4E). Adult female mice in the osteoporosis group exhibited a 47.9% reduction in femoral and tibial trabecular bone volume compared to those in the sham group over the 8 weeks. Interestingly, supplementation with M2-EVs through tail vein injection attenuated trabecular bone loss. The ratio of the trabecular bone volume to the total volume fraction (BV/TV) was 56.5% greater in the M2-EVs treatment group than in the osteoporosis group (Figure 4F). Consistent with these findings, the M2-EV group exhibited moderate increases of 52.7% and 24.4% in bone mineral density (BMD) and trabecular thickness (Tb.Th), accompanied by a 19.4% reduction in trabecular separation (Tb.Sp) compared to the control group (Figure 4F). Similarly, ELISA showed that M2-EVs decreased the concentration of serum TRACP 5b (Figure 4G).

Consistent with the micro-CT findings, Masson staining revealed that new bone formation was markedly increased in the M2-EVs group.[24] In contrast, only a small amount of new bone was formed in the group not treated with EVs (Figure 4H). Furthermore, significant donor-derived $TRAP^+$ osteoclastic areas were observed in the M2-EVs group (Figure 4I). Moreover, immunofluorescence staining revealed that M2-EVs injection contributed to a significant increase in the level of ARG-1 and a marginal decrease in the level of NFATc1 in the bone tissue (Figure 4J). In addition to attenuating bone loss, M2-EVs also enhanced bone fracture healing in mice. H&E staining and Masson staining showed that M2-EVs promoted bone repair in bone defects (Figure 4K).

M2-EVs significantly increase the oxidative phosphorylation (OXPHOS) of OCPs to produce an M2 macrophage-like metabolic pattern

Transcriptome sequencing was performed to obtain a more comprehensive gene expression profile of OCPs (immature OCs), OCPs

Figure 3. M2-EVs transform OCPs into M2 macrophage-like cells

(A) M2-EVs were labeled with the green fluorescent cell linker PKH67 and taken up by PKH26 labeled-BMMs and BMSCs. M2-EVs were stained green, BMMs were stained red, and BMSCs were observed under a bright field (boxed in white). Scale bar, 200 μm. (B) Schematic diagram of the stimulation time window. (C) Western blot analysis of CD206 protein expression on different days of OC differentiation. (D) Quantitative real-time PCR of OC and M2 macrophage marker expression on different days of OC differentiation (n = 3). *p < 0.05, **p < 0.01, ***p < 0.001, ****p < 0.0001, compared with 9 days group, #p < 0.05, ##p < 0.01, ###p < 0.001, ####p < 0.0001 compared with the OC group without M2-EVs. (E) TRAP staining, immunofluorescence staining for TRAP, and semiquantitative analysis of cells treated with or without RANKL and/or M2-EVs. The mixture was incubated for 5 days. Scale bar, 200 μm. (F) Western blot analysis and qualification of TRAP, NFATc1, ARG-1, and CD206. (G) Quantitative real-time PCR was performed to analyze the expression of OC and M2 macrophage-specific markers (n = 3). (H) Resorption activity of OCs on bovine bone slices under scanning electron microscopy (SEM; boxed in white) or toluidine blue staining (boxed in white) after treatment with or without RANKL and/or M2-EVs and semiquantification on day 9. Scale bar, 30 μm (SEM), 200 μm (toluidine blue stain). The red areas indicate areas of bone resorption via SEM, and the white spots indicate the areas where bone resorption occurred according to toluidine blue staining. (I) The migratory and tube-forming capacities of human umbilical vein endothelial cellss were assessed following exposure to CM derived from OCPs treated with or without RANKL and/or M2-EVs. Scale bar, 500 μm. One-way ANOVA with Tukey's multiple comparisons test (A and D–H).

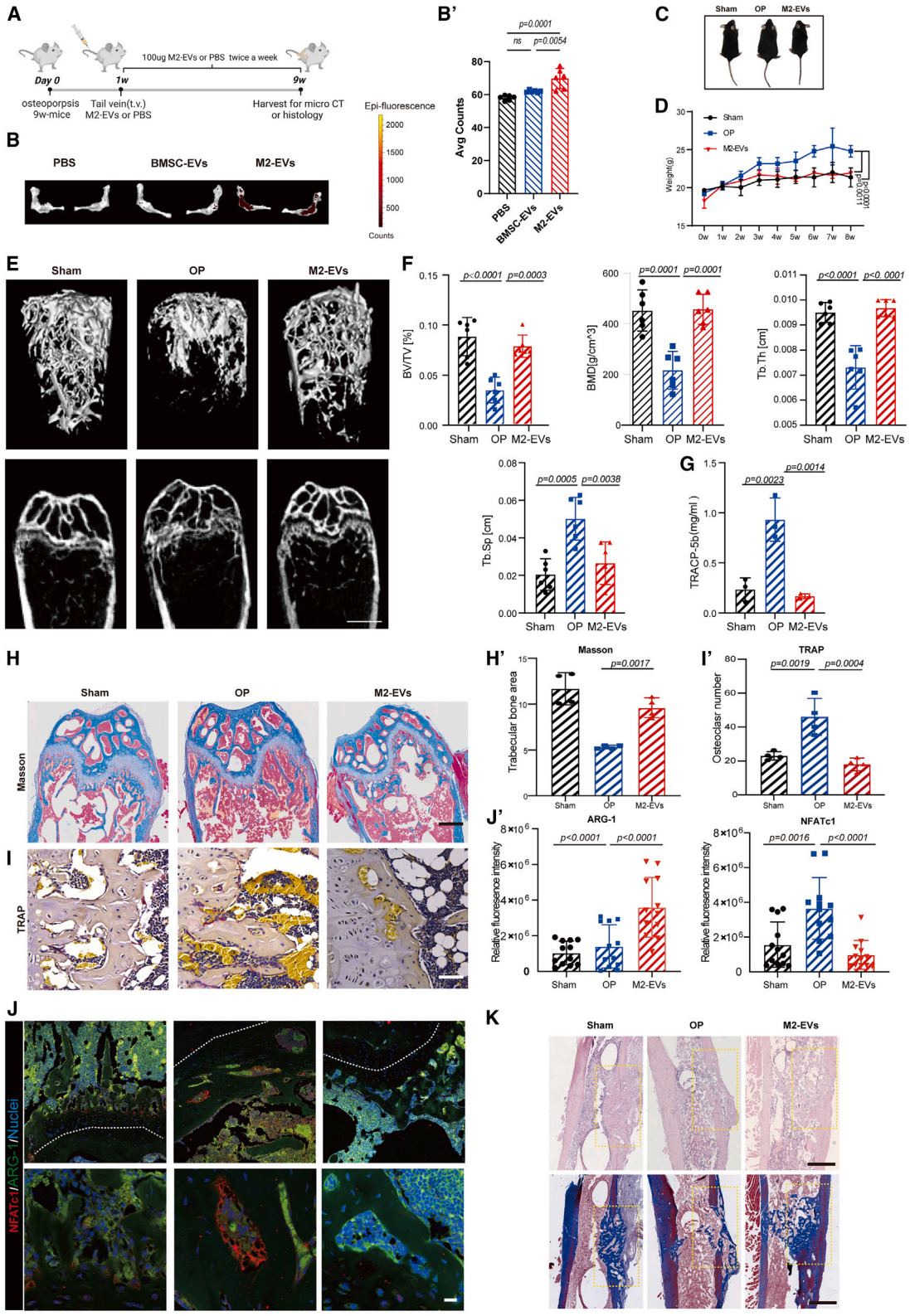

(legend on next page)

cultured with RANKL (mature OCs), and OCPs cultured with RANKL and M2-EVs (Figure 5A). Consistent with the results above, transcriptomic analysis revealed that M2-EVs downregulated OC marker expression and upregulated M2 marker expression (Figure 5B). Notably, changes in intrinsic cellular mechanisms typically accompany changes in cell phenotype-related gene expression. Gene Ontology analysis revealed that the five most enriched biological processes were "cellular process," "biological process," "regulation of biological process," "response to stimulus," and "metabolic process" (Figure 5C). Furthermore, single-cell RNA sequencing (scRNA-seq) data analysis revealed that metabolism-related genes were downregulated with age (Figure S6). These results suggest that M2-EVs treatment is an optimal strategy for preventing and controlling senescent bone-related cells from a metabolic perspective.

OXPHOS is dramatically altered during the process of OC differentiation.[25,26] Therefore, we detected several mitochondrial indices, including the mitochondrial membrane potential and MitoSOX concentration. According to the JC-1 staining results, red fluorescence reflected a greater mitochondrial membrane potential, whereas green fluorescence reflected a lower mitochondrial membrane potential. The results showed that the OC with M2-EVs displayed greater membrane potential than mature OC. In addition, M2-EVs decreased MitoSOX levels and increased MitoTracker levels (Figures 5D and 5E). The flow cytometry data for MitoSOX staining were consistent with the above results (Figure 5F). To further examine the mitochondrial content after M2-EVs treatment, TEM was used to observe the approximate number and morphology of the intracellular mitochondria. After M2-EVs treatment, the mitochondria exhibited an obviously elongated morphology and increased number of mitochondria (Figures 5G and 5H). Mitochondria, which are key energy-producing cytoplasmic organelles and important regulators of metabolic homeostasis,[27] form hubs for the hormonal regulation of lipid metabolism and OXPHOS to meet cellular energy demands. The observed changes in mitochondria suggested that the OCPs underwent metabolic alterations. A Seahorse assay was also used to determine the basal oxygen consumption rate (OCR), maximal OCR, ATP-linked OCR, and spare respiratory capacity in OCPs (immature OCs), OCPs with RANKL (mature OCs), and OCPs with RANKL and M2-EVs. All of the oxygen consumption rates were lower in OCs without M2-EVs stimulation (Figures 5I and 5J). The result of MitoTracker and OCR indicated that OCPs with RANKL have reduced mitochondrial membrane potential and mass, but exhibited increased OCR used for ATP production.[28] The results showed a significant increase in the mitochondrial OCR after M2-EVs treatment, indicating that M2-EVs inhibit OC formation by improving OXPHOS activity.

M2-EVs participate in glutamine metabolism to enhance mitochondrial biological reactions

To determine the specific mechanisms underlying the regulation of the OCP phenotype and metabolism by M2-EVs, we conducted targeted metabolomics analysis of the M0-EV and M2-EVs contents. Figure 6A shows the 18 candidates with the most significant differences between M0-EVs and M2-EVs. The three predominant metabolite molecules were pantothenic acid, 1-hexadecanoyl-*sn*-glycero-3-phosphoethanolamine, and L-glutamic acid. Kyoto Encyclopedia of Genes and Genomes (KEGG) analysis revealed that the enriched biological functions involved amino acid metabolism, especially D-glutamine and D-glutamate metabolism (Figure 6B), consistent with the bubble plot. These results suggest that glutamine metabolism plays a role in the M2-EV-mediated cell fate transition. Glutamine is first hydrolyzed by glutaminase (GLS) into ammonia and glutamate, which are subsequently further metabolized to αKG via glutamate dehydrogenase (GDH). Notably, the anaplerotic reaction replenishes the tricarboxylic acid (TCA) cycle with αKG. To further characterize the alteration in glutamine metabolism in the TCA cycle after M2-EVs treatment, we measured both the intracellular glutamate concentration and GDH activity. As expected, the L-glutamate level was significantly increased after M2-EVs treatment. The same overall tendency was observed for GDH. In addition, the level of αKG, the primary product of glutamine metabolism, was also increased after M2-EVs treatment (Figure 6C). Western blot analysis of GDH and GLS1 levels in OCPs also confirmed the enzyme activity results (Figure 6D). These results suggested that M2-EVs increased the number of M2 macrophages, which in turn increase the ratio of M2 macrophages to OCs (the M2/OC ratio). To elucidate the impact of molecular constituents on the phenotype of OCPs, we added glutamine metabolism inhibitor R162 during macrophage polarization and the function of M2-EVs was weakened via quantitative real-time PCR and Western blot (Figures S7A and S7B). Then, electroporation experiments were conducted to eliminate RNA from the EVs,[29] and TEM demonstrated that EVs exhibited normal morphology. We unexpectedly found that M2-EVs also function in the absence of RNA via quantitative real-time PCR. We can say that RNA does not function as the main active substance, and metabolites (glutamate) are vital in the phenotypic characteristics of OCPs (Figures 6E, 6F, and S7C). These results suggested that M2-EVs increase the number of M2 macrophages, which in turn increases the

Figure 4. M2-EVs rescue osteoporosis and contribute to the formation of a femur morphological pattern that closely resembles the physiological norm

(A) Schematic diagram. (B and B') BMSC-EVs and M2-EVs were labeled with the near-infrared fluorophore to detect sensitivity and depth, and the fluorescence quantification has been quantified (B'). (C and D) The animals werephotographed (C) and weighed every week (D). (E) The microarchitecture of the trabecular portion of the proximal femur of mice was measured and analyzed with a micro-CT machine. Scale bar, 500 μm. (F) Quantitative micro-CT analysis of the BV/TV, BMD, Tb.Th, and Tb.Sp (n = 6). (G) The concentration of serum TRACP-5b was measured via ELISA (n = 3). (H, H' and I) Masson staining (H) and TRAP staining (I) at 8 weeks. The blue color indicates newly formed bone and the red color is mature bone tissue. The mean amount of newly formed bone tissue was determined, and $TRAP^+$ multinuclear cells were counted (H'). Scale bars, 500 μm (above) and 50 μm (below). (J and J') Immunofluorescence double staining of the femoral metaphysis with antibodies against NFATc1 and ARG-1(J) and quantification of the immunofluorescence intensity of tissue sections stained with antibodies (J'). Scale bar, 50 μm. (K) H&E staining and Masson staining after bone defect repair in the sham, osteoporosis, and osteoporosis with M2-EVs treatment groups. Scale bar, 500 μm. One-way ANOVA with Tukey's multiple comparisons test (B', D, F, G, H', I', and J').

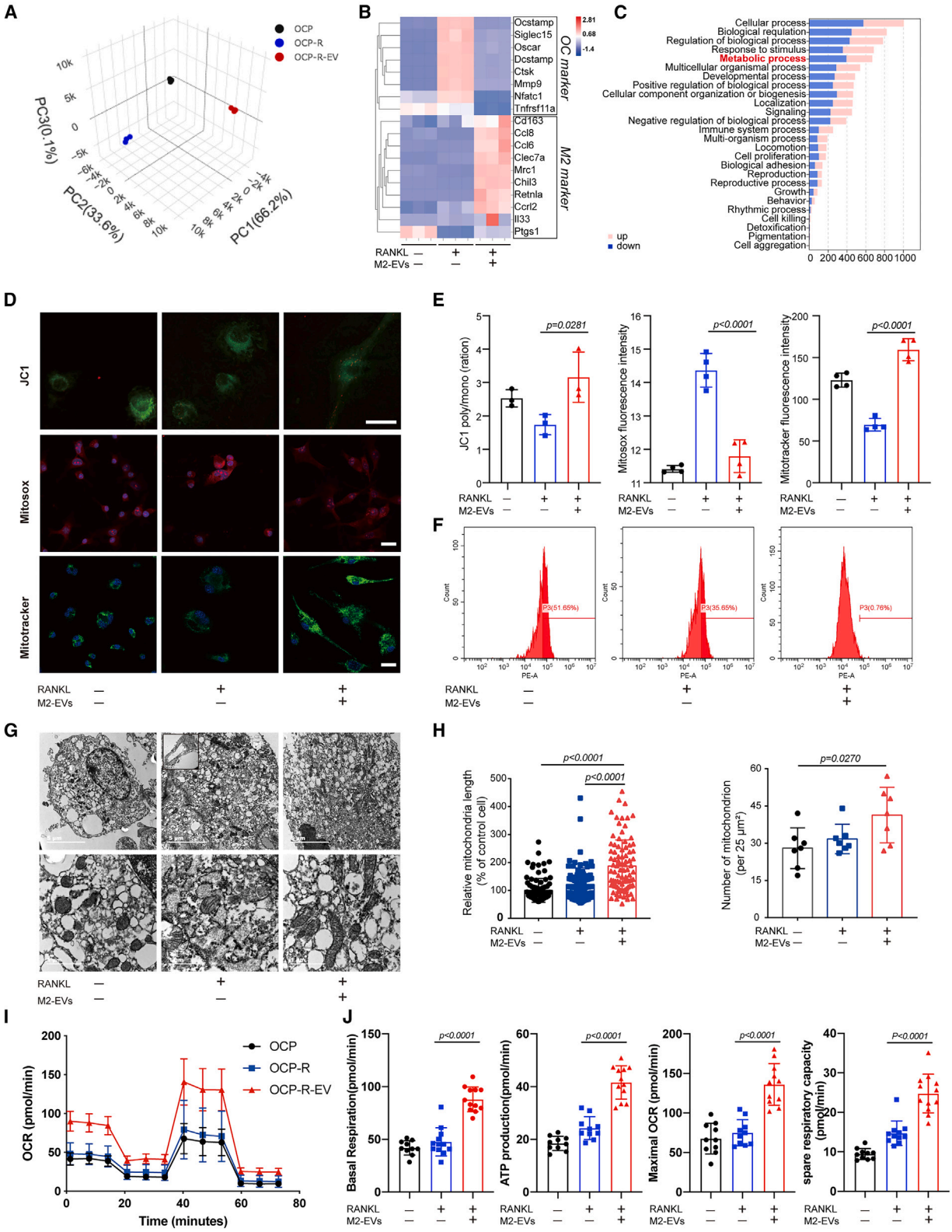

(legend on next page)

ratio of M2 macrophages to OCs (the M2/OC ratio) via glutamine metabolism. We further used the GLS inhibitor R162 to decrease glutamine degradation and αKG synthesis, and dimethyl (DM)-αKG was used as an alternative to M2-EVs. Western blot results showed that the substitution of M2-EVs with DM-αKG reversed the promoting effect of R162 (Figure 6G). Cell morphology was confirmed by TRAP staining and immunofluorescence staining, and ARG-1 expression was inhibited. The results showed that the GDH inhibitor R162 promoted mature OC growth (Figure 6H). The quantitative real-time PCR results were also consistent with the cell morphology staining (Figure 6I).

The results demonstrated that M2-EVs were enriched with metabolites that participate in glutamine metabolism to initiate OCP fate transition, but the link remained correlative. Therefore, we developed an experimental workflow using stable isotope labeling of amino acids in cell culture to perform an unsupervised analysis of glutamine transfer to recipient OCP cells by M2-EVs (Figure 7A). In OCPs exposed to M2-EVs (which carry ^{13}C-labeled glutamine), ^{13}C-labeled isotopes were detected for glutamine metabolites (α-KG, L-glutamate and L-glutamine) and TCA cycle metabolites (succinic acid, fumaric acid, L-malic acid) (Figure 7B). Furthermore, females from osteoporosis or sham surgery animal models were stained both red (GDH) and green (ARG-1), and the results showed that the expression of these genes increased after M2-EVs treatment, which means the coexpression of GDH indicated that GDH was coexpressed with ARG-1 (Figure 7C). Our results indicate that glutamate is predominantly enriched in M2-EVs and that M2-EVs can effectively transfer glutamine to target OCPs to alter their phenotype and function to an M2 macrophage-like pattern.

M2-EVs carry a product of glutamine metabolism, αKG, which functions in regulating epigenetic modifications

Research has already shown that αKG activates macrophages via alternative pathways (M2), including fatty acid oxidation and Jmjd3-dependent epigenetic reprogramming[30,31] and that the level of histone 3 lysine 27 trimethylation (H3K27me3) on the Nfatc1 gene in BMMs is markedly reduced in mature OCs. We next explored whether M2-EVs play similar roles in modulating chromatin directly by regulating the activity of chromatin-transacting proteins via histone-modifying enzymes. The expression of key developmental genes tends to be regulated by the trimethylation of histone 3 lysine 9 (H3K9me3) and H3K27me3, so H3K27me3 and H3K9me3 levels were tested (Figure 8A). Western blot analysis revealed that M2-EVs significantly upregulated H3K27me3 demethylation in OCPs, whereas H3K9me3 levels remained unchanged (Figures 8B and 8C).

Next, we performed immunofluorescence staining for NFATc1, a crucial marker of OC differentiation. M2-EVs administration increased the proportion of NFATc1$^+$ cells *in vivo*, indicating relative compression of the mature OC population. Notably, the percentage of OCPs that were double labeled for NFATc1 and H3K27me3 was significantly greater than that in the other two control groups (Figure 8D). Conversely, double staining for ARG-1 and H3K27me3 was decreased after M2-EVs treatment (Figure 8E). To further substantiate the above results, we performed chromatin immunoprecipitation (ChIP) experiments based on the RNA-seq results. Consistent with the finding that H3K27me3 is a transcriptional repressor, the ChIP experiments demonstrated that M2-EVs treatment increased H3K27me3 occupancy at the promoters of Mmp9 and Ntatc1 while decreasing occupancy at the promoters of Retnla and Mrc1 (Figures 8F and 8G). These findings suggest that the inhibitory effect of M2-EVs on OC differentiation depends at least partly on the regulation of histone modifications, possibly because M2-EVs carry αKG to function.

DISCUSSION

The present study revealed a previously unrecognized mechanism by which M2-EVs reestablish the balance between OCs and M2 macrophages as well as a preventive effect of M2-EVs on bone loss. In this study, we found that M2-EV-derived glutamate induced macrophage reprogramming to reduce age-related inflammation, as reflected by decreases in the expression of genes typifying the OC lineage and increases in the expression of genes that are specific to M2 macrophages. Targeting glutamine metabolism by integrating metabolic networks and epigenetic modifications revealed unexpected roles for glutamate and αKG, the primary products of glutamine metabolism, in the fate transitions of OCPs.

OCs, which are absorbent cells in bone, play pivotal roles in bone remodeling. Increased OC activity is predominant in postmenopausal osteoporosis patients and primarily affects trabecular bones, leading to a relatively rapid decline in bone density. This finding suggested that the ovariectomy animal model is more suitable than the other models.[32,33] Regulatory strategies are now focused on inhibiting RANKL-stimulated OCP fusion or promoting apoptosis.[34–36] However, close neighboring cells or noncells around target cells are inevitably affected, which disrupts the homeostasis of the intracellular environment. The skeletal cell lineage includes hematopoietic cells,

Figure 5. High OXPHOS induces OCPs to exhibit an M2 macrophage-like metabolic pattern

(A and B) Principal-component analysis (A) and heatmap (B) of the mean abundance of OC and M2 markers in OCPs treated with or without RANKL and/or M2-EVs. (C) GO enrichment pathway analysis. (D–F) Mitochondrial membrane potential was determined by dual JC-1 staining, and the production of mitoROS was measured by MitoSOX fluorescence (D) and semiquantitative analysis (E). MitoSOX was detected by flow cytometry (F). Scale bar, 25 μm. (G and H) Mitochondria were detected via TEM. Scale bar, 6 μm; enlargement, 1 μm (G). Quantitative analyses of the number of mitochondria per area and mitochondrial length (H). (I and J) OCPs were treated with or without RANKL and/or M2-EVs, and mitochondrial OXPHOS reactions and respiration were assessed with a Seahorse XF96 Analyzer (I). Quantification of basal respiration, ATP-linked respiration, maximal respiratory capacity, and spare respiratory capacity (J). One-way ANOVA with Tukey's multiple comparisons test (E, H, and J).

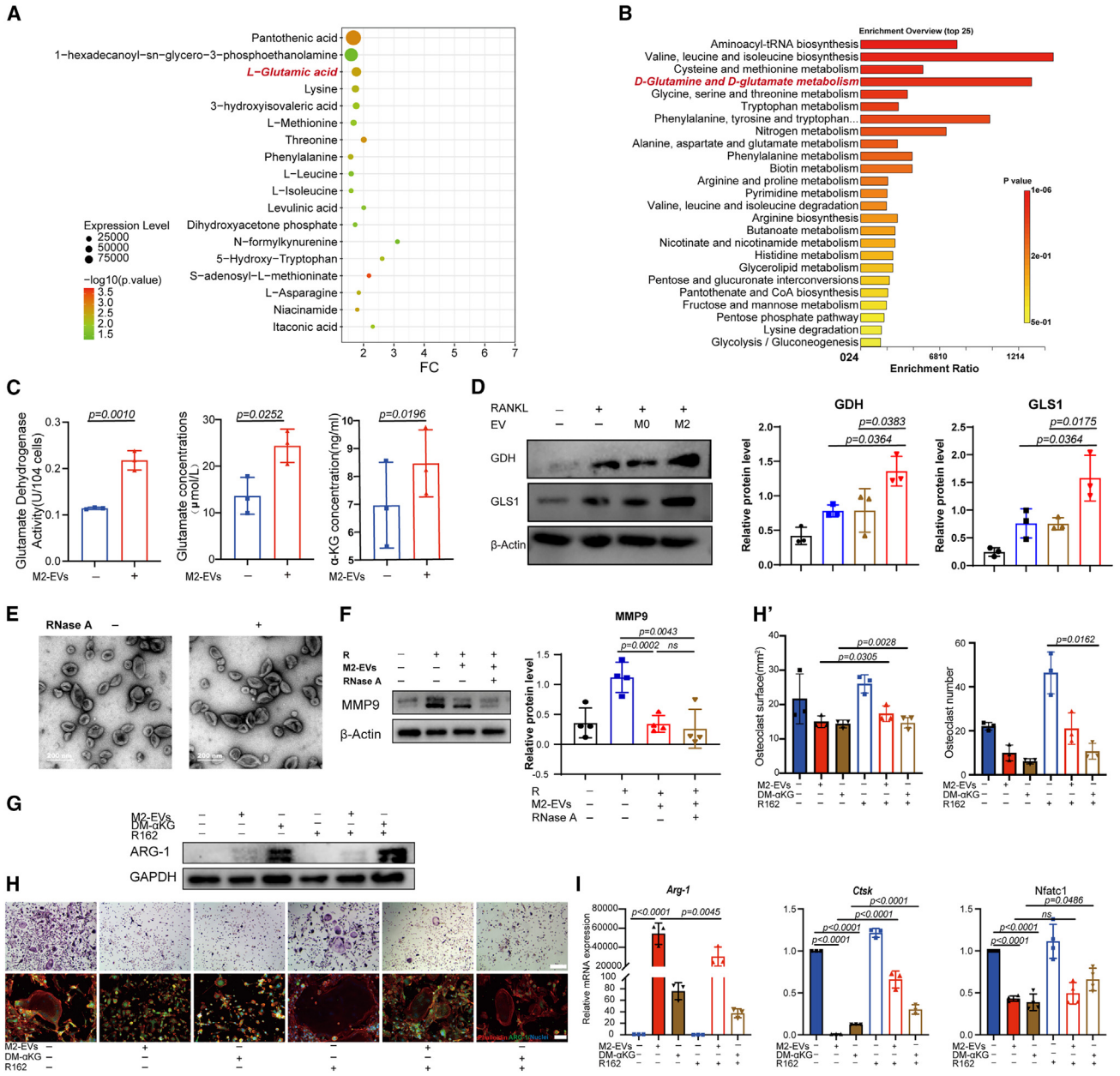

Figure 6. M2-EVs enhance glutamine metabolism

(A) Bubble chart of the results of the metabolite analyses. (B) Pathway enrichment analysis of differentially modulated metabolites. (C) Detection of intracellular GDH activity and glutamate and αKG concentrations in OCPs treated with or without RANKL and/or M2-EVs (n = 3). (D) Western blot analysis of GDH and GLS1 levels after M2-EVs treatment and semiquantitative analysis (n = 4). (E) Representative TEM images of the M2-EVs and M2-EVs without RNA. (F) Western blot and quantitative real-time PCR analysis of matrix metalloproteinase 9 (MMP9) expression under stimulation of M2-EVs and M2-EVs without RNA (n = 4). (G) Western blot analysis of the protein expression of OC or M2 marker genes in the presence or absence of the GDH inhibitor R162. (H and H') Representative TRAP staining and double-staining images showing the actin cytoskeleton in M2-EV-stimulated OCPs under various culture conditions and semiquantified (H') on day 7 (n = 3); scale bar, 100 μm (above) and 50 μm (below). (I) Quantitative real-time PCR analysis of the mRNA expression OC or M2 marker genes in the presence or absence of the GDH inhibitor R162 (n = 3). Student's t test (C); One-way ANOVA with Tukey's multiple comparisons test (C, D, F, H′, and I).

stromal cells, endothelial cells, and chondrocytes, and both skeletal stem cells (SSCs) and macrophages share a common BM niche to participate in close cell-to-cell communication. Our result is based on a previous study in which we identified six cluster subpopulations with transcriptomic profiles that differed in subtle ways and to focus on monocyte/macrophages to make a causal inference. Single-cell

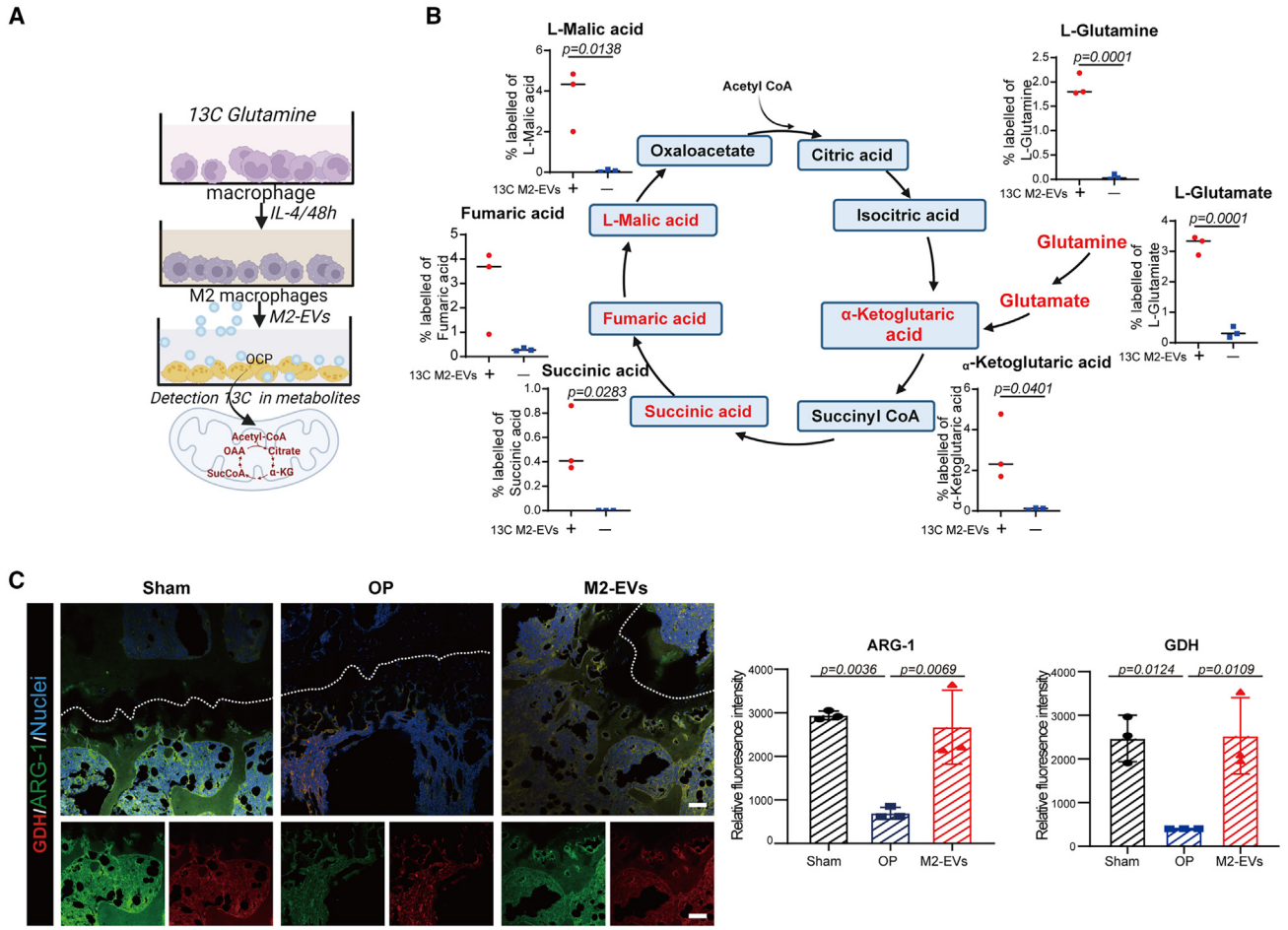

Figure 7. Glutamate-containing EVs participate in OCPs metabolism

(A and B) Schematic illustration (A) and metabolic tracing (B) used to verify that glutamine is synthesized. (C) Immunofluorescence double staining of GDH and ARG-1 in a sham surgery with PBS, an osteoporosis surgery with PBS, and an osteoporosis surgery with M2-EVs and quantification of the immunofluorescence intensity of tissue sections stained with antibodies. Student's t test (B); One-way ANOVA with Tukey's multiple comparisons test (C).

analysis revealed that M2 marker expression decreased and that OC marker expression increased with age. The trajectory tree revealed that 0- and 2-month-old cells tended to aggregate at the M2 branches of the trajectory tree, whereas 24-month-old cells accumulated at the OC branches of the tree. This suggested that senescence may result in an imbalance between OCs and M2 macrophages, which translates to more OCs and fewer M2 macrophages. Here, OCPs were determined to represent critical physiological periods with remarkable plasticity, consistent with previous findings, which would facilitate the downregulation of OC-specific genes.[34,37] In this study, we stimulated the transformation of OCPs into M2-like macrophages via M2-EVs to maintain homeostasis. Thus, we propose a strategy to transform bone-resorbing cells into bone-repairing cells with age.

Owing to their composition, EVs can be used as shuttles of drugs and carry molecules toward specific cells. Therefore, EVs are being exploited for prognosis as biomarkers and in innovative therapies.[38] Distinct modifications within the microenvironment elicit a range of inducible and reversible metabolic programs via EVs, leading to the activation of functional phenotypes.[39] This highlights the significant associations between EVs, the glycolytic-driven immunosuppressive niche, the transmission of hypoxia-inducible factor -1α-stabilizing long noncoding RNA, and the regenerative neurogenesis-angiogenesis cycle.[40–42] In fact, their properties, such as biocompatibility and low immunogenicity, make EVs ideal for maintaining bone homeostasis. There is a broad consensus that M2-derived EVs are part of the intercellular signaling network that enhances tissue repair. However, most of the studies on M2-EVs have focused on promoting BMSC osteogenic differentiation and reducing adipogenesis and osteoclastogenesis via miRNAs.[43,44] Chen et al. reported that M2-Exos could upregulate the cytokine IL-10 in BMSCs and BM-derived macrophages by delivering exosomal IL-10 mRNA to improve alveolar resorption.[45] Kim et al. reported an EV-guided cell reprogramming technique to directly convert M1 to M2

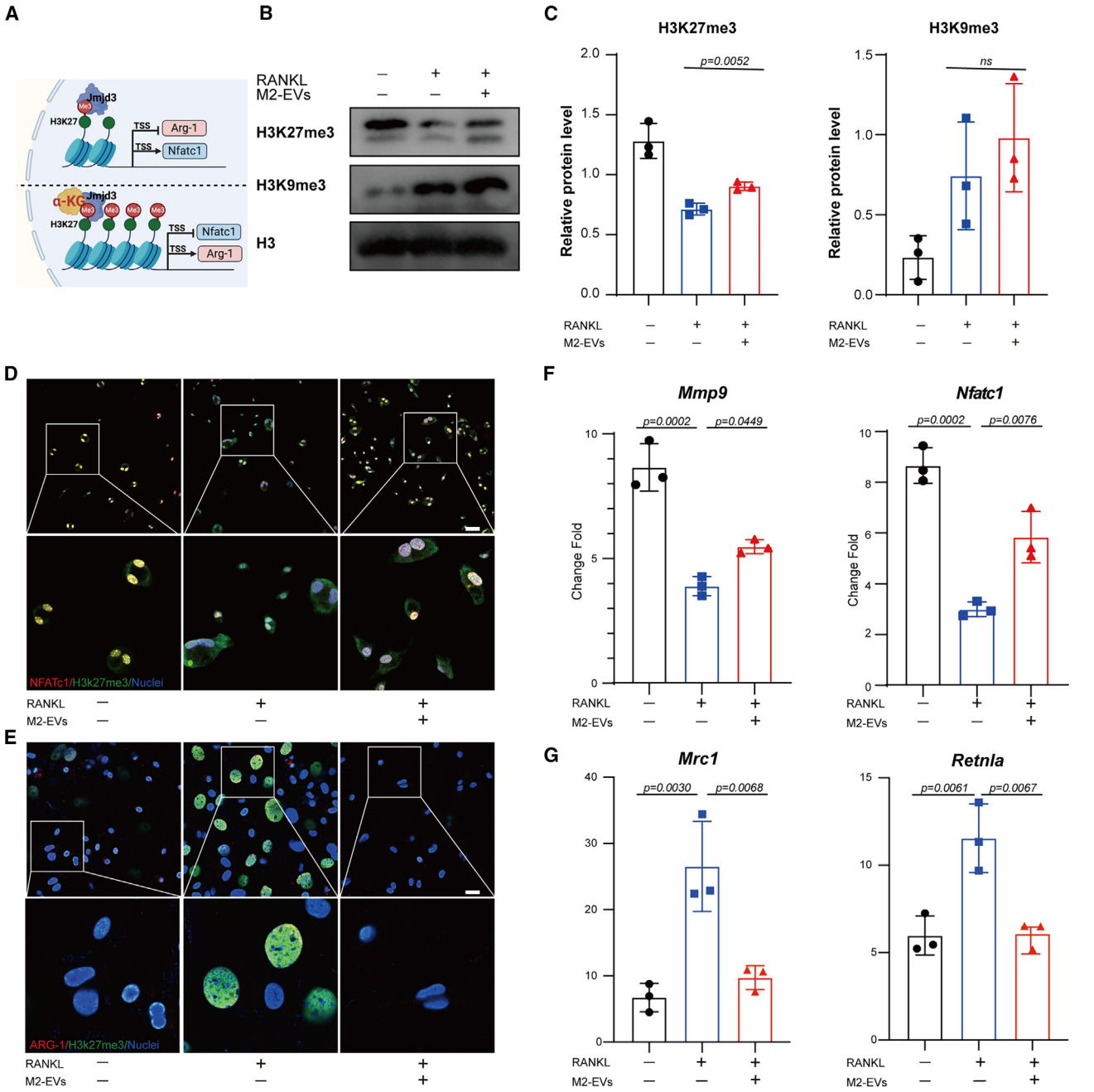

Figure 8. Glutamate-containing M2-EVs function by generating αKG to regulate epigenetic modifications

(A) Schematic diagram. (B and C) Western blot analyses of H3K27me3 and H3K9me3 methylation sites (B) and semiquantitative analysis (C). (D and E) Nuclear colocalization of H3K27me3 with NFATc1 (D) or ARG-1 (E) was detected by immunofluorescence confocal microscopy and semiquantitative analysis (n = 3). Scale bar, 200 μm. (F and G) ChIP analysis of H3K27me3 in BMMs stimulated with or without M2-EVs after quantitative real-time PCR analysis of the promoter regions of the OC (F) and M2 (G) marker genes (n = 3). One-way ANOVA with Tukey's multiple comparisons test (C, F, and G).

macrophages in wound healing.[13] In addition, M2-EVs showed better bone-targeting capacity than BMSC-EVs, as evidenced by the high contrast biodistribution of M2-EVs compared with BMSC-EVs *in vivo* fluorescence images obtained at 12 h after tail vein injection. In addition, the function of M0-EVs also has been considered, although we observed a discrepancy between the upregulation of Nfatc1 mRNA expression and the downregulation of NFATc11 protein expression in the M0-EV-treated group compared to the no-EV group.[46,47] We

concluded that M0-EVs have the potential to enhance the differentiation of OCPs into OCs at the transcriptional level. And OCPs treated with M0-EVs exhibit a strong ability to inhibit the formation of multinucleated, mature OCs, possibly due to the influence of posttranscriptional factors. Therefore, in this study, we developed M2-EVs as delivery tools for targeting the OCP pathway to modulate energy balance and bone homeostasis.

Furthermore, in addition to morphological and gene expression modifications, metabolic pathways undergo significant alterations during the process of OC differentiation.[48] Immature OCs, or OCPs, exhibit a state of heightened metabolic activity driven primarily by OXPHOS, whereby mitochondria generate the majority of the ATP necessary to support OC proliferation.[49] Impeding ATP production through the use of inhibitors targeting mitochondrial complexes or ATP synthase has been shown to impede osteoclastogenesis.[50] Subsequently, increased glycolytic activity facilitates macromolecular biosynthesis and precisely coordinates it with the acquisition of bone-resorbing activity in mature OCs.[48,51] Thus, OCs can determine the direction of metabolic flux according to functional demands. An emerging body of literature indicates that some cells can transfer their mitochondria or metabolites to other cell types to support their metabolic fitness via EVs.[52–54] As a branch of OXPHOS, glutamine metabolism is emerging as an intriguing regulatory node.[55] Here, we found that M2-EVs could transport glutamate, a metabolite, into OCPs to drive glutamine metabolism and subsequently promote OXPHOS. The metabolic flux of ^{13}C revealed that the metabolic pathway was active and oriented glutamine metabolism toward OXPHOS.

The initiation of glutamine metabolism is facilitated by the enzyme GLS, which catalyzes the deamination of glutamine to generate glutamate, a crucial intermediate metabolite used to power the mitochondrial TCA cycle, amino acid synthesis, and glutathione biosynthesis.[55,56] αKG, an anti-inflammatory metabolite of glutamine metabolism, is a cofactor for both Jmjds and the TET family of DNA demethylases to control the metabolic reprogramming of M2 macrophages.[57] H3K27me3 on the Nfatc1 gene in BMMs is markedly reduced in mature OCs.[58] An increase in glutamine-derived αKG is predicted to enhance DNA and histone demethylation to potentially regulate OC lineage commitment by targeting H3K27me3 in Nfatc1, which is contrary to what occurs in the Arg-1 gene. Here, we uncovered a mode of communication between metabolic reprogramming and epigenetic modifications that transforms OCP fate and has implications for skeletal metabolism.

Our results indicate that natural M2-EVs are highly biocompatible bone-targeting nanoparticles that can achieve efficient bone-targeted delivery. After endocytosis, OCPs switch into M2-like macrophages to attenuate bone resorption and enhance bone repair via glutamate upregulation. M2-derived EVs not only act on monocyte-macrophage phenotypic switching but also influence surrounding cells through paracrine secretion to create an activated environment. Since the EV-guided monocyte-macrophage phenotype switch is a dual strategy involving OCPs and M2 macrophages, M2-EVs treatment is a promising therapeutic strategy for the treatment of various diseases associated with an imbalance between OBs and OCs. In our study, we demonstrated the effective ability of M2-EVs to induce cell fate transition and the potential of M2-EVs for osteoporosis treatment, showing that M2-EVs offer distinct advantages due to their compatibility, bioactivity, and immunogenicity for the treatment of bone resorption diseases.

MATERIALS AND METHODS

OC differentiation

BMMs were isolated from the tibias and femurs of 6-, 18-, or 48-week-old male C57BL/6J mice (Shanghai SLAC Laboratory Animal) by flushing the BM cavity. The cells were incubated with minimum essential medium-alpha (α-MEM; Cienry, CR-11900) supplemented with 10% fetal bovine serum (FBS; Gibco, catalog no. 044) and M-CSF (20 ng/mL; R&D Systems, catalog no. 416-ML) for 2 days. The nonadherent cells were harvested and further cultured for 2 days in α-MEM containing M-CSF to generate BMMs. Then, the BMMs were seeded into 24-well plates (4×10^4 cells/well) or 96-well plates (1×10^4 cells/well) and cultured for 7–9 days in the presence of M-CSF and RANKL (100 ng/mL; R&D Systems, catalog no. 462-TEC). The medium was changed every 2 days. BMMs were cultured for 2 days in the presence of M-CSF and RANKL to maintain OCPs, after which the medium was replaced with α-MEM supplemented with 10% FBS and M-CSF.

BMSC isolation

Mouse BMSCs were isolated from both the femurs and tibias of 6-week-old female C57BL/6J mice and pooled to obtain a single-cell suspension. Then, the BMSCs were cultured and purified in α-MEM supplemented with 10% FBS. Cells from passage 2 were used in these experiments.

Live/dead assay

To determine the percentage of dead cells at the time of M2-EVs harvest, a calcein- acetoxymethyl ester (AM)/propidium iodide (PI) staining kit (BestBio, catalog no. BB-4126) was used to determine the ratios of live (calcein-AM+PI−) to dead (calcein-AM−PI+) cells. The live cells and dead cells were counted, and the survival rate was calculated by dividing the number of live cells by the total number of cells. In addition, the cells were stained with 7-amino-actinomycin D (7-AAD) (BD Biosciences, catalog no. 559925) according to the manufacturer's instructions, and the 7-AAD cells were defined as live cells.

Isolation of M2-EVs

The isolation and identification of M2-EVs were performed as described previously.[14] Briefly, when the Raw264.7 cells (Meisen, catalog no. CTCC-001-0048) reached 80%–90% confluence, the culture medium was replaced with serum-free medium. The cells were cultured for 12 h, and the culture media was completely removed and replaced with 10 ng/mL IL-4 serum-free media to eliminate nonadherent cells. The 48-h stimulation allowed them to differentiate into M2 macrophages. To compare the effects of EVs isolated from

M2 macrophages after 48-h induction with IL-4, the CM was initially collected and subsequently supplemented with serum-free media for an additional 48 h. The CM from M2 macrophages was collected and centrifuged at 300 × *g* for 10 min, 2,000 × *g* for 10 min, and 10,000 × *g* for 30 min at 4°C to remove dead cells and cellular debris. The supernatant was subsequently filtered through a Steritop 0.22-μm filter sterilizer (Millipore, catalog no. SLHV033RB). Ultracentrifugation was performed twice using a 70 Ti rotor (Beckman) at 100,000 × *g* for 70 min at 4°C, and the pellet was then resuspended in 200 μL PBS. The protein concentration in the EV suspension was determined using a bicinchoninic acid protein assay kit. NTA of EVs was performed using ZetaView (Malvern NanoSight NS500). The default settings were used for the NTA analysis, including a detection threshold of 12, an automatic blue size, and an automatic maximum jump distance ranging from 12.7 to 14.0 pixels. The morphology of the EVs was observed via TEM (Thermo FEI Tecnai G2 spirit 120 kV).

Nano-flow cytometry analysis

To assess the concentration and absolute size distribution of the EVs, the EVs were resuspended in PBS after ultracentrifugation. After being treated with 1% Triton X-100, EVs were detected with a flow nanoanalyzer (NanoFCM). To identify the surface markers of the EVs, the EVs were labeled at a concentration of approximately 1,010 particles/mL, in which 9 μL of the sample was added to 1 μL diluted 10-fold dilutions of CD163, CD206, CD81, and CD9. The mixture was incubated at 37°C for 30 min and then diluted 100 times with PBS before analysis on the Nano Analyzer. The EVs were detected at small threshold settings (68–155 S16M-Exos), and the labeled population was analyzed via the fluorescein isothiocyanate or phycoerythrin channel. The results were validated through at least three replicates.

Cellular uptake of M2-EVs by BMMs and BMSCs

The fluorescent dye PKH67 (10 μM; Sigma-Aldrich) was added to the M2-EVs suspension, which was incubated for 4 min at room temperature. The stained EVs were washed with PBS via ultracentrifugation at 100,000 × *g* for 70 min, after which the pellet was resuspended in PBS. BMMs (2×10^4 cells/well) were stained with PKH26 and cocultured with the same number of BMSCs. PKH26-labeled BMMs and unlabeled BMSCs were incubated with PKH67-labeled M2-EVs (10 μg/mL; green labeled with PKH67) for 24 h. Images were acquired every hour using a high-content screening system (Thermo Scientific CellInsight CX7 LZR).

EV electroporation

These EVs were extracted using ultracentrifugation and then electroporated using a CUY21EDITII system. For RNase treatment, purified exosomes were incubated (37°C, 30 min) with 2 mg/mL protease-free RNase A (Thermo Scientific) followed by the addition of 10× concentrated RNase inhibitor (Ambion). The EVs were then washed with cold PBS twice before ultracentrifugation at 100,000 × *g* for 60 min. The concentration of RNA in the EVs was determined using a Takara MiniBEST Universal RNA Extraction Kit to determine the CD260/280 ratio to confirm the removal of RNA.

Quantitative real-time PCR

Total RNA was isolated from cells using TRIzol reagent (Invitrogen, catalog no. 15596018); 2 μg RNA was reverse transcribed into cDNA using PrimeScript RT Master Mix (Takara, catalog no. RR037A). Quantitative real-time PCR was carried out with a CFX384 Real-Time PCR Detection System (Bio-Rad) in a 10-μL reaction volume using a TB Green Premix Ex Taq II Kit (Takara, catalog no. RR420B). Normalized mRNA quantities were determined with the comparative cycle threshold method, and the glyceraldehyde 3-phosphate dehydrogenase mRNA level was used as an internal reference control. The sequences of the PCR primers used are listed in Table S2.

Western blot analysis

Western blotting was performed as described previously.[59] Briefly, 50 μg protein isolated from the supernatant of cells was separated by SDS-PAGE (10%) and transferred onto polyvinylidene fluoride membranes. After blocking with 5% skim milk powder in Tris-buffered saline with 0.1% Tween 20 detergent for 1 h, the proteins adsorbed on the membranes were probed with the following primary antibodies: anti-ARG-1 (Cell Signaling Technology, catalog no. 2171), anti-Alix (Cell Signaling Technology, catalog no. 2171), anti-annexin V (Cell Signaling Technology, catalog no. 8555), anti-flotillin-1 (Cell Signaling Technology, catalog no. 18634), anti-CD9 (Cell Signaling Technology, catalog no. 13174), anti-CD54 (Cell Signaling Technology, catalog no. 67836), anti-GM130 (Cell Signaling Technology, catalog no. 12480), anti-calnexin (Cell Signaling Technology, catalog no. 2679), anti-TRAP (GeneTex, catalog no. GTX100438), anti-NFATc1 (Abcam, catalog no. ab25916), anti-RANK (Abcam, catalog no. ab19140), anti-MMP9 (Cell Signaling Technology, catalog no. 13667), anti-CD206 (Biorbyt, catalog no. orb4941), anti-H3 (Cell Signaling Technology, catalog no. 4620), anti-H3K27me3 (Cell Signaling Technology, catalog no. 9733), anti-H3K9me3 (HUABIO, catalog no. 1112-3), anti-GDH (Cell Signaling Technology, catalog no. 12793S), anti-GLS1 (Cell Signaling Technology, catalog no. 56750S) anti-GAPDH (Proteintech, catalog no. 60004-1) and anti-β-Actin (Servicebio, catalog no. GB11001) were used as loading controls. The membranes were incubated with primary antibodies at 4°C overnight. Horseradish peroxidase (HRP)-conjugated goat anti-mouse and HRP-conjugated goat anti-rabbit secondary antibodies (Servicebio, catalog no. GB23303) were also used. The proteins on the membranes were observed and detected using an enhanced chemiluminescence system (Bio-Rad).

TRAP staining

TRAP staining was conducted using a TRAP Stain Kit (Sigma, catalog no. 387) according to the manufacturer's instructions. The nuclei were counterstained with H&E for 1 min at room temperature and then washed with large amounts of water. Then, the $TRAP^+$ cells were counted under an optical microscope (200× magnification). The images were analyzed and quantified using ImageJ software version 6.0 (NIH).

Immunofluorescence

In brief, cells were fixed with 4.0% paraformaldehyde in PBS for 20 min. After washing with PBS three times, the cells were permeabilized using 0.5% (v/v) Triton X-100 for 15 min, blocked in 5% BSA (Solarbio, catalog no. A8020) for 1 h, and then washed again. Primary antibodies were added overnight, after which the membranes were incubated with secondary antibodies. The nuclei were stained with DAPI at room temperature for 5 min or 30 s. Finally, the cells were washed with PBS, observed under a confocal fluorescence microscope (Leica), and quantified with ImageJ software version 6.0.

Bone resorption activities

The resorptive function of the mature OCs derived from the RANKL-differentiated BMMs was analyzed on sterile bovine bone slices, which were placed in 96-well plates with three replicates for each condition. Bone slices were soaked in 75% ethanol overnight and then switched to fresh medium. BMMs were seeded at 10^4 cells/well onto bovine bone slices. The cells were treated with or without M2-EVs after treatment with 100 ng/mL RANKL for 2 days to induce OC differentiation. After 7 days of culture (the medium was changed every 48 h), all of the cells were removed from the bone slices, and the resorption pits were then visualized under a scanning electron microscope (Nova Nano 450) or optical microscope after toluidine blue staining (Olympus). The total number and area of resorption pits were quantified and compared using ImageJ software version 6.0.

MitoSOX staining and analysis

Mitochondrial reactive oxygen species levels were analyzed using MitoSOX Red (Invitrogen, catalog no. M36008). Cultures were incubated with 5 μM MitoSOX for 30 min at 37°C and washed twice with warm PBS. After Hoechst 33342 (1 μg/mL; Thermo Fisher Scientific) was added to the cells, fluorescence images were taken with a Leica confocal microscope. The cells were rinsed with cold PBS and analyzed using a CytoFLEX LX flow cytometer (Beckman).

JC-1 staining and analysis

The mitochondrial membrane potential was measured by incubating the cells with JC-1 in PBS for 20 min at 37°C. The other methods used were the same as those used for MitoROS analysis.

Metabolic assays

The OCR was measured in OCPs using an XF96 extracellular flux analyzer as described previously (Seahorse Bioscience, Agilent). Briefly, isolated OCPs were plated in a cell culture microplate at 10^4 cells/well. Before the assay, the RPMI 1640 medium was removed and replaced with 200 μL assay medium. The cells were preincubated under these conditions for 1 h at 37°C in air. The OCPs were sequentially exposed to the mitochondrial respiratory complex inhibitors oligomycin (1.5 μM), carbonyl cyanide-4-(trifluoromethoxy) phenylhydrazone (2 μM), and rotenone (1 μM) plus antimycin A (1 μM). The OCRs of the cells were quantified and plotted as described previously.

Measurement of αKG concentrations in cultured cells

The αKG concentrations were analyzed via high-performance liquid chromatography (HPLC). Differentiated OCPs (5×10^4/mL) were treated with M2-EVs (100 μg/mL) for 3 days and then washed with 0.9% NaCl. Samples were then extracted with liquid chromatography-mass spectrometry (LC-MS)-grade methanol:acetonitrile:water at 50:30:20 (v/v/v) (1 mL/10^6 cells) and centrifuged at 12,000 rpm at 4°C for 15 min. The supernatants were transferred to HPLC glass vials for LC-MS analysis, and αKG (>99% purity; Aladdin Biotech, catalog no. K105570) was used as a standard.

Targeted metabolomics analysis

M0-EVs and M2-EVs were collected as previously described. A 50-μL sample was transferred to a new centrifuge tube and mixed with 250 μL 20% acetonitrile/methanol. The mixture was vortexed for 3 min and then centrifuged at 12,000 rpm for 10 min at 4°C. Next, 250 μL of the supernatant was transferred to a tube and chilled at −20°C for 30 min. After centrifugation at 12,000 rpm for another 10 min at 4°C, the supernatant was placed in a well plate for LC-MS/MS analysis. All of the metabolites were detected and analyzed by MetWare (http://www.metware.cn/) based on the AB Sciex QTRAP 6500 LC-MS/MS platform.

Metabolic flux analysis

The samples were mixed with ice-cold 80% methanol in water, incubated for 30 min at 1,500 rpm at 4°C, and then centrifuged for 10 min at 12,000 rpm at 4°C. The supernatant was removed into a clean 1.5-mL centrifuge tube and dried using a SpeedVac. The dried extracts were redissolved in 2% acetonitrile in water, and the upper layer of liquid was collected for LC-MS analysis. The LC-MS parameters were based on a previous method.[60,61] An ACQUITY UPLC HSS T3 1.8-μm, 3.0 × 100-mm column (Waters) was used for reverse-phase chromatographic analysis, and an ACQUITY UPLC BEH Amide 1.7-μm, 2.1 × 100-mm column (Waters) was used for normal-phase chromatographic analysis. An ultraperformance liquid chromatograph (Agilent 1290 II) coupled to a quadrupole-time-of-flight mass spectrometer (AB SCIEX, 5600 Triple TOF Plus) was used to acquire metabolomics data.

RNA-seq analysis

Total RNA was extracted as previously described. The RNA quality was assessed with an Agilent 2100 Bioanalyzer (Agilent Technologies) and via RNase-free agarose gel electrophoresis. Eukaryotic mRNA was enriched with oligo(dT) beads after RNA assessment. The enriched mRNA was subsequently fragmented into short fragments with fragmentation buffer and reverse transcribed into cDNA with an NEBNext Ultra RNA Library Prep Kit for Illumina (NEB, catalog no. 7530). Double-stranded cDNA was subsequently purified, end-repaired, A-tailed, and ligated to Illumina sequencing adapters. The products were purified with AMPure XP Beads (1.0×). The ligated fragments were cleaned and subjected to size selection by agarose gel electrophoresis and PCR.

Measurement of GDH activity and glutamate concentrations

GDH activity and glutamate concentrations were analyzed using a GDH and Glutamate Assay Kit (Nanjing Jiancheng Bioengineering Institute, catalog nos. A125-1-1 and A074-1-1). A total of 1×10^4 cells were lysed in 1 mL of ice-cold GDH assay buffer and ultrasonicated at 30% power. The samples were centrifuged at 8,000 × *g* for 10 min at 4°C, after which the supernatants were extracted. Supernatant 50 μL was mixed with 950 μL of buffer and incubated at 37°C for 20 s, after which the initial absorbance at 370 nm was measured. Further incubation at 37°C was conducted for 5 min, and the reading was repeated. Glutamate concentration analysis was performed with an analysis kit according to the instructions in a manner similar to that used for GDH activity analysis.

Experimental animals

Eight-week-old female C57BL/6 mice were purchased from Shanghai SLAC Laboratory Animal Center and housed in the Zhejiang Chinese Medical University Laboratory Animal Facility. The mice were provided a standard rodent chow diet and water *ad libitum*. The plants were maintained under a 12-h light/12-h dark cycle at 20°C–25°C and 60% relative humidity. The mice were allowed to acclimatize for 1 week before the experiments commenced. All of the animal experiments were approved by the Institutional Animal Care and Use Committee of Zhejiang Chinese Medical University and complied with the Guide for the Care and Use of Laboratory Animals (ZJU20220173). For ovariectomy experiments, 9-week-old female C57BL/6 mice were anesthetized by intraperitoneal injection of 1% pentobarbital sodium and were subjected to sham surgery or bilateral ovariectomy to induce osteoporosis, as described previously. Penicillin was intramuscularly administered to the mice every day for 3 days beginning at 3 days postsurgery. The mice were sacrificed for analysis after intervention for 8 weeks.

Biophotonic imaging analysis

M2-EVs and BMSC-EVs were labeled with VivoTrack-680 (Beijing Fluorescence Biotechnology), and the labeled EVs were intravenously injected into 8-week-old female C57BL/6 mice (100 μg/100 μL per mouse). The mice were killed at 12 h after injection, and the bones were excised and analyzed. Finally, fluorescence imaging was conducted to determine the distribution of the labeled EVs using a Living Image System (Caliper Life Science).

Micro-CT analysis

Bilateral tibias were fixed in 4% formaldehyde solution for preservation and scanned by micro-CT using a Milabs U-CT-XUHR with an 8-μm pixel size, 166-kV source voltage, 60-μA current, and 0.25-mm aluminum filter. Milabs software version 1.4.4 was used to reconstruct whole-bone images, and the lengths of the proteins were measured. The regions analyzed were approximately 2 mm distal to the growth plate in the trabecular bone and proximal/middle (37% of the length of the bone from its proximal end) in the cortical bone of the tibia. Three-dimensional structural analyses of these trabecular and cortical bone sites were performed using SkyScan software version 1.6.1.1. We evaluated the BMD (g/cm^3), BV/TV (%), Tb.Th (mm), Tb.Sp (cm), and trabecular number (1/cm) in the trabecular bone in the cortical bones.

Immunohistochemistry

Femurs from mice euthanized 8 weeks after EV injection were obtained, soft tissue was removed, and the tissues were fixed in 4% paraformaldehyde for 2 days. The bones were decalcified in EDTA and embedded in paraffin according to standard procedures. Slides of paraffin-embedded bone (5 μm) were deparaffinized, rehydrated with alcohol gradients, and repaired in antigen repair solution for 10 min. After washing with Tris-buffered saline (pH 7.6), the slides were blocked with 10% normal goat serum (Proteintech Group, catalog no. B900780) for 1 h at room temperature and then incubated with primary antibodies overnight at 4°C.

DATA AND CODE AVAILABILITY

All of the data are available in the main text or the supplemental information.

SUPPLEMENTAL INFORMATION

Supplemental information can be found online at https://doi.org/10.1016/j.ymthe.2024.02.005.

ACKNOWLEDGMENTS

This work was supported by the National Natural Science Foundation of China (grant no. 82270964) and the Zhejiang Basic Public Welfare Research Project (no. Y24H140003). The *in vivo* study was approved by the Ethics Committee for Animal Research at Zhejiang University (ethics approval no. ZJU20220173). All of the procedures were conducted in accordance with the standard guidelines and the Declaration of Helsinki.

AUTHOR CONTRIBUTIONS

Conceptualization: X.H. and Y.L. Investigation: X.H., Y.L., J.S., Y.Z., and W.W. Data curation: J.M. Formal analysis: Y.W. Writing – original draft: X.H., Y.L., and J.S. Writing – review & editing: Z.X. and Z.C. Visualization: X.Z. Project administration: Z.X. and Z.C. Supervision: Z.X. and Z.C.

DECLARATION OF INTERESTS

The authors declare no competing interests.

REFERENCES

1. Ambrosi, T.H., Marecic, O., McArdle, A., Sinha, R., Gulati, G.S., Tong, X., Wang, Y., Steininger, H.M., Hoover, M.Y., Koepke, L.S., et al. (2021). Aged skeletal stem cells generate an inflammatory degenerative niche. Nature *597*, 256–262. https://doi.org/10.1038/s41586-021-03795-7.

2. Coppé, J.P., Desprez, P.Y., Krtolica, A., and Campisi, J. (2010). The senescence-associated secretory phenotype: the dark side of tumor suppression. Annu. Rev. Pathol. *5*, 99–118. https://doi.org/10.1146/annurev-pathol-121808-102144.

3. Liang, W., Chen, Q., Cheng, S., Wei, R., Li, Y., Yao, C., Ouyang, Z., Kang, D., Chen, A., Liu, Z., et al. (2022). Skin chronological aging drives age-related bone loss via secretion of cystatin-A. Nat. Aging *2*, 906–922. https://doi.org/10.1038/s43587-022-00285-x.

4. Liu, X.S., Stein, E.M., Zhou, B., Zhang, C.A., Nickolas, T.L., Cohen, A., Thomas, V., McMahon, D.J., Cosman, F., Nieves, J., et al. (2012). Individual trabecula segmentation (ITS)-based morphological analyses and microfinite element analysis of HR-pQCT images discriminate postmenopausal fragility fractures independent of DXA measurements. J. Bone Miner. Res. *27*, 263–272. https://doi.org/10.1002/jbmr.562.

5. Saito, H., Gasser, A., Bolamperti, S., Maeda, M., Matthies, L., Jähn, K., Long, C.L., Schlüter, H., Kwiatkowski, M., Saini, V., et al. (2019). TG-interacting factor 1 (Tgif1)-deficiency attenuates bone remodeling and blunts the anabolic response to parathyroid hormone. Nat. Commun. *10*, 1354. https://doi.org/10.1038/s41467-019-08778-x.

6. Boyle, W.J., Simonet, W.S., and Lacey, D.L. (2003). Osteoclast differentiation and activation. Nature *423*, 337–342. https://doi.org/10.1038/nature01658.

7. Cioni, B., Zaalberg, A., van Beijnum, J.R., Melis, M.H.M., van Burgsteden, J., Muraro, M.J., Hooijberg, E., Peters, D., Hofland, I., Lubeck, Y., et al. (2020). Androgen receptor signalling in macrophages promotes TREM-1-mediated prostate cancer cell line migration and invasion. Nat. Commun. *11*, 4498. https://doi.org/10.1038/s41467-020-18313-y.

8. Mantovani, A., Sica, A., Sozzani, S., Allavena, P., Vecchi, A., and Locati, M. (2004). The chemokine system in diverse forms of macrophage activation and polarization. Trends Immunol. *25*, 677–686. https://doi.org/10.1016/j.it.2004.09.015.

9. Gao, S., Mao, F., Zhang, B., Zhang, L., Zhang, X., Wang, M., Yan, Y., Yang, T., Zhang, J., Zhu, W., et al. (2014). Mouse bone marrow-derived mesenchymal stem cells induce macrophage M2 polarization through the nuclear factor-kappaB and signal transducer and activator of transcription 3 pathways. Exp. Biol. Med. *239*, 366–375. https://doi.org/10.1177/1535370213518169.

10. Zhao, S.J., Kong, F.Q., Jie, J., Li, Q., Liu, H., Xu, A.D., Yang, Y.Q., Jiang, B., Wang, D.D., Zhou, Z.Q., et al. (2020). Macrophage MSR1 promotes BMSC osteogenic differentiation and M2-like polarization by activating PI3K/AKT/GSK3beta/beta-catenin pathway. Theranostics *10*, 17–35. https://doi.org/10.7150/thno.36930.

11. Liu, F., Qiu, H., Xue, M., Zhang, S., Zhang, X., Xu, J., Chen, J., Yang, Y., and Xie, J. (2019). MSC-secreted TGF-beta regulates lipopolysaccharide-stimulated macrophage M2-like polarization via the Akt/FoxO1 pathway. Stem Cell Res. Ther. *10*, 345. https://doi.org/10.1186/s13287-019-1447-y.

12. Clement, E., Lazar, I., Attané, C., Carrié, L., Dauvillier, S., Ducoux-Petit, M., Esteve, D., Menneteau, T., Moutahir, M., Le Gonidec, S., et al. (2020). Adipocyte extracellular vesicles carry enzymes and fatty acids that stimulate mitochondrial metabolism and remodeling in tumor cells. EMBO J. *39*, e102525. https://doi.org/10.15252/embj.2019102525.

13. Kim, H., Wang, S.Y., Kwak, G., Yang, Y., Kwon, I.C., and Kim, S.H. (2019). Exosome-Guided Phenotypic Switch of M1 to M2 Macrophages for Cutaneous Wound Healing. Adv. Sci. *6*, 1900513. https://doi.org/10.1002/advs.201900513.

14. Lan, Y., Xie, H., Jin, Q., Zhao, X., Shi, Y., Zhou, Y., Hu, Z., Ye, Y., Huang, X., Sun, Y., et al. (2022). Extracellular vesicles derived from neural EGFL-Like 1-modified mesenchymal stem cells improve acellular bone regeneration via the miR-25-5p-SMAD2 signaling axis. Bioact. Mater. *17*, 457–470. https://doi.org/10.1016/j.bioactmat.2022.01.019.

15. Lan, Y., Jin, Q., Xie, H., Yan, C., Ye, Y., Zhao, X., Chen, Z., and Xie, Z. (2020). Exosomes Enhance Adhesion and Osteogenic Differentiation of Initial Bone Marrow Stem Cells on Titanium Surfaces. Front. Cell Dev. Biol. *8*, 583234. https://doi.org/10.3389/fcell.2020.583234.

16. Goddard, M.E., and Whitelaw, E. (2014). The use of epigenetic phenomena for the improvement of sheep and cattle. Front. Genet. *5*, 247. https://doi.org/10.3389/fgene.2014.00247.

17. Ishii, M., Wen, H., Corsa, C.A.S., Liu, T., Coelho, A.L., Allen, R.M., Carson, W.F., 4th, Cavassani, K.A., Li, X., Lukacs, N.W., et al. (2009). Epigenetic regulation of the alternatively activated macrophage phenotype. Blood *114*, 3244–3254. https://doi.org/10.1182/blood-2009-04-217620.

18. Teitelbaum, S.L. (2000). Bone resorption by osteoclasts. Science *289*, 1504–1508. https://doi.org/10.1126/science.289.5484.1504.

19. Dai, E., Han, L., Liu, J., Xie, Y., Kroemer, G., Klionsky, D.J., Zeh, H.J., Kang, R., Wang, J., and Tang, D. (2020). Autophagy-dependent ferroptosis drives tumor-associated macrophage polarization via release and uptake of oncogenic KRAS protein. Autophagy *16*, 2069–2083. https://doi.org/10.1080/15548627.2020.1714209.

20. Kronstadt, S.M., Van Heyningen, L.H., Aranda, A., and Jay, S.M. (2023). Assessment of anti-inflammatory bioactivity of extracellular vesicles is susceptible to error via media component contamination. Cytotherapy *25*, 387–396. https://doi.org/10.1016/j.jcyt.2022.12.002.

21. Théry, C. (2011). Exosomes: secreted vesicles and intercellular communications. F1000 Biol. Rep. *3*, 15. https://doi.org/10.3410/B3-15.

22. Anesi, A., Generali, L., Sandoni, L., Pozzi, S., and Grande, A. (2019). From Osteoclast Differentiation to Osteonecrosis of the Jaw: Molecular and Clinical Insights. Int. J. Mol. Sci. *20*, 4925. https://doi.org/10.3390/ijms20194925.

23. Lee, S., Liu, P., Ahmad, M., Tuckermann, J.P., Choi, W.S., and You, J.S. (2021). Glutamine metabolite alpha -ketoglutarate acts as an epigenetic co-factor to interfere with osteoclast differentiation. Bone *145*, 115843. https://doi.org/10.1016/j.bone.2020.115836.

24. Huang, W., Cheng, S., Wang, X., Zhang, Y., and Zhang, L. (2021). Noncompressible Hemostasis and Bone Regeneration Induced by an Absorbable Bioadhesive Self久ealing Hydrogel. Adv. Funct. Mater. *31*. https://doi.org/10.1002/adfm.202009189.

25. Busse, E., Simkin, J., Marrero, L., Stewart, K., Brunauer, R., Muneoka, K., Guntur, A., Lacey, M., and Sammarco, M. (2019). Sirtuin 3 deficiency does not impede digit regeneration in mice. Sci. Rep. *9*, 16491. https://doi.org/10.1038/s41598-019-52921-z.

26. Lemma, S., Sboarina, M., Porporato, P.E., Zini, N., Sonveaux, P., Di Pompo, G., Baldini, N., and Avnet, S. (2016). Energy metabolism in osteoclast formation and activity. Int. J. Biochem. Cell B *79*, 168–180. https://doi.org/10.1016/j.biocel.2016.08.034.

27. Ma, L., Wang, H., Wang, C., Su, J., Xie, Q., Xu, L., Yu, Y., Liu, S., Li, S., Xu, Y., and Li, Z. (2016). Failure of Elevating Calcium Induces Oxidative Stress Tolerance and Imparts Cisplatin Resistance in Ovarian Cancer Cells. Aging Dis. *7*, 254–266. https://doi.org/10.14336/Ad.2016.0118.

28. Man, K., Gabriel, S.S., Liao, Y., Gloury, R., Preston, S., Henstridge, D.C., Pellegrini, M., Zehn, D., Berberich-Siebelt, F., Febbraio, M.A., et al. (2017). Transcription Factor IRF4 Promotes CD8+ T Cell Exhaustion and Limits the Development of Memory-like T Cells during Chronic Infection. Immunity *47*, 1129–1141.e5. https://doi.org/10.1016/j.immuni.2017.11.021.

29. Zhang, G., Huang, X., Xiu, H., Sun, Y., Chen, J., Cheng, G., Song, Z., Peng, Y., Shen, Y., Wang, J., and Cai, Z. (2020). Extracellular vesicles: Natural liver-accumulating drug delivery vehicles for the treatment of liver diseases. J. Extracell. Vesicles *10*, e12030. https://doi.org/10.1002/jev2.12030.

30. Liu, P.S., Wang, H., Li, X., Chao, T., Teav, T., Christen, S., Di Conza, G., Cheng, W.C., Chou, C.H., Vavakova, M., et al. (2017). alpha-ketoglutarate orchestrates macrophage activation through metabolic and epigenetic reprogramming. Nat. Immunol. *18*, 985–994. https://doi.org/10.1038/ni.3796.

31. Yasui, T., Hirose, J., Tsutsumi, S., Nakamura, K., Aburatani, H., and Tanaka, S. (2011). Epigenetic Regulation of Osteoclast Differentiation: Possible Involvement of Jmjd3 in the Histone Demethylation of Nfatc1. J. Bone Miner. Res. *26*, 2665–2671. https://doi.org/10.1002/jbmr.464.

32. Duque, G., and Troen, B.R. (2008). Understanding the mechanisms of senile osteoporosis: new facts for a major geriatric syndrome. J. Am. Geriatr. Soc. *56*, 935–941. https://doi.org/10.1111/j.1532-5415.2008.01764.x.

33. Jesserer, H. (1953). [Involutional osteoporosis]. Z. Rheumaforsch. *12*, 261–291.

34. Ye, S., Fujiwara, T., Zhou, J., Varughese, K.I., and Zhao, H. (2016). LIS1 Regulates Osteoclastogenesis through Modulation of M-SCF and RANKL Signaling Pathways and CDC42. Int. J. Biol. Sci. *12*, 1488–1499. https://doi.org/10.7150/ijbs.15583.

35. Udagawa, N., Koide, M., Nakamura, M., Nakamichi, Y., Yamashita, T., Uehara, S., Kobayashi, Y., Furuya, Y., Yasuda, H., Fukuda, C., and Tsuda, E. (2021). Osteoclast differentiation by RANKL and OPG signaling pathways. J. Bone Miner. Metab. *39*, 19–26. https://doi.org/10.1007/s00774-020-01162-6.

36. Tai, T.W., Chen, C.Y., Su, F.C., Tu, Y.K., Tsai, T.T., Lin, C.F., and Jou, I.M. (2017). Reactive oxygen species are required for zoledronic acid-induced apoptosis in osteoclast precursors and mature osteoclast-like cells. Sci. Rep. *7*, 44245. https://doi.org/10.1038/srep44245.

37. Hayashi, M., Nakashima, T., Taniguchi, M., Kodama, T., Kumanogoh, A., and Takayanagi, H. (2012). Osteoprotection by semaphorin 3A. Nature *485*, 69–74. https://doi.org/10.1038/nature11000.

38. Milbank, E., Dragano, N.R.V., González-García, I., Garcia, M.R., Rivas-Limeres, V., Perdomo, L., Hilairet, G., Ruiz-Pino, F., Mallegol, P., Morgan, D.A., et al. (2021). Small extracellular vesicle-mediated targeting of hypothalamic AMPK alpha 1 corrects obesity through BAT activation. Nat. Metab. *3*, 1415–1431. https://doi.org/10.1038/s42255-021-00467-8.

39. Xiong, Y., Mi, B.B., Lin, Z., Hu, Y.Q., Yu, L., Zha, K.K., Panayi, A.C., Yu, T., Chen, L., Liu, Z.P., et al. (2022). The role of the immune microenvironment in bone, cartilage, and soft tissue regeneration: from mechanism to therapeutic opportunity. Mil. Med. Res. *9*, 65. https://doi.org/10.1186/s40779-022-00426-8.

40. Chen, F., Chen, J., Yang, L., Liu, J., Zhang, X., Zhang, Y., Tu, Q., Yin, D., Lin, D., Wong, P.P., et al. (2019). Extracellular vesicle-packaged HIF-1alpha-stabilizing lncRNA from tumour-associated macrophages regulates aerobic glycolysis of breast cancer cells. Nat. Cell Biol. *21*, 498–510. https://doi.org/10.1038/s41556-019-0299-0.

41. Morrissey, S.M., Zhang, F., Ding, C., Montoya-Durango, D.E., Hu, X., Yang, C., Wang, Z., Yuan, F., Fox, M., Zhang, H.G., et al. (2021). Tumor-derived exosomes drive immunosuppressive macrophages in a pre-metastatic niche through glycolytic dominant metabolic reprogramming. Cell Metab. *33*, 2040–2058.e10. https://doi.org/10.1016/j.cmet.2021.09.002.

42. Xiong, Y., Lin, Z., Bu, P., Yu, T., Endo, Y., Zhou, W., Sun, Y., Cao, F., Dai, G., Hu, Y., et al. (2023). A Whole-Course-Repair System Based on Neurogenesis-Angiogenesis Crosstalk and Macrophage Reprogramming Promotes Diabetic Wound Healing. Adv. Mater. *35*, e2212300. https://doi.org/10.1002/adma.202212300.

43. Li, Z., Wang, Y., Li, S., and Li, Y. (2021). Exosomes Derived From M2 Macrophages Facilitate Osteogenesis and Reduce Adipogenesis of BMSCs. Front. Endocrinol. *12*. https://doi.org/10.3389/fendo.2021.680328.

44. Xiong, Y., Chen, L., Yan, C.C., Zhou, W., Yu, T., Sun, Y., et al. (2021). M2 Macrophagy-derived exosomal miRNA-5106 induces bone mesenchymal stem cells towards osteoblastic fate by targeting salt-inducible kinase 2 and 3 (vol 18, 66, 2020). J. Nanobiotechnology *19*. https://doi.org/10.1186/s12951-021-00828-1.

45. Chen, X., Wan, Z., Yang, L., Song, S., Fu, Z., Tang, K., Chen, L., and Song, Y. (2022). Exosomes derived from reparative M2-like macrophages prevent bone loss in murine periodontitis models via IL-10 mRNA. J. Nanobiotechnology *20*, 110. https://doi.org/10.1186/s12951-022-01314-y.

46. Lin, X., Chai, G., Wu, Y., Li, J., Chen, F., Liu, J., Luo, G., Tauler, J., Du, J., Lin, S., et al. (2023). Retraction Note: RNA m6A methylation regulates the epithelial mesenchymal transition of cancer cells and translation of Snail. Nat. Commun. *14*, 7424. https://doi.org/10.1038/s41467-023-43307-x.

47. Buccitelli, C., and Selbach, M. (2020). mRNAs, proteins and the emerging principles of gene expression control. Nat. Rev. Genet. *21*, 630–644. https://doi.org/10.1038/s41576-020-0258-4.

48. Park-Min, K.H. (2019). Metabolic reprogramming in osteoclasts. Semin. Immunopathol. *41*, 565–572. https://doi.org/10.1007/s00281-019-00757-0.

49. Wang, J., Guan, H., Liu, H., Lei, Z., Kang, H., Guo, Q., Dong, Y., Liu, H., Sun, Y., Fang, Z., and Li, F. (2020). Inhibition of PFKFB3 suppresses osteoclastogenesis and prevents ovariectomy-induced bone loss. J. Cell. Mol. Med. *24*, 2294–2307. https://doi.org/10.1111/jcmm.14912.

50. Kim, J.M., Jeong, D., Kang, H.K., Jung, S.Y., Kang, S.S., and Min, B.M. (2007). Osteoclast precursors display dynamic metabolic shifts toward accelerated glucose metabolism at an early stage of RANKL-Stimulated osteoclast differentiation. Cell. Physiol. Biochem. *20*, 935–946. https://doi.org/10.1159/000110454.

51. Indo, Y., Takeshita, S., Ishii, K.A., Hoshii, T., Aburatani, H., Hirao, A., and Ikeda, K. (2013). Metabolic Regulation of Osteoclast Differentiation and Function. J. Bone Miner. Res. *28*, 2392–2399. https://doi.org/10.1002/jbmr.1976.

52. Clement, E., Lazar, I., Attané, C., Carrié, L., Dauvillier, S., Ducoux-Petit, M., Esteve, D., Menneteau, T., Moutahir, M., Le Gonidec, S., et al. (2020). Adipocyte extracellular vesicles carry enzymes and fatty acids that stimulate mitochondrial metabolism and remodeling in tumor cells. Embo J. *39*, e102525. https://doi.org/10.15252/embj.2019102525.

53. Ikeda, G., Santoso, M.R., Tada, Y., Li, A.M., Vaskova, E., Jung, J.H., O'Brien, C., Egan, E., Ye, J., and Yang, P.C. (2021). Mitochondria-Rich Extracellular Vesicles From Autologous Stem Cell-Derived Cardiomyocytes Restore Energetics of Ischemic Myocardium. J. Am. Coll. Cardiol. *77*, 1073–1088. https://doi.org/10.1016/j.jacc.2020.12.060.

54. Chen, Q.T., Zhang, Z.Y., Huang, Q.L., Chen, H.Z., Hong, W.B., Lin, T., Zhao, W.X., Wang, X.M., Ju, C.Y., Wu, L.Z., et al. (2022). HK1 from hepatic stellate cell-derived extracellular vesicles promotes progression of hepatocellular carcinoma. Nat. Metab. *4*, 1306–1321. https://doi.org/10.1038/s42255-022-00642-5.

55. Yu, Y., Newman, H., Shen, L., Sharma, D., Hu, G., Mirando, A.J., Zhang, H., Knudsen, E., Zhang, G.F., Hilton, M.J., and Karner, C.M. (2019). Glutamine Metabolism Regulates Proliferation and Lineage Allocation in Skeletal Stem Cells. Cell Metab. *29*, 966–978.e4. https://doi.org/10.1016/j.cmet.2019.01.016.

56. van Gastel, N., and Carmeliet, G. (2021). Metabolic regulation of skeletal cell fate and function in physiology and disease. Nat. Metab. *3*, 11–20. https://doi.org/10.1038/s42255-020-00321-3.

57. McDonough, M.A., Loenarz, C., Chowdhury, R., Clifton, I.J., and Schofield, C.J. (2010). Structural studies on human 2-oxoglutarate dependent oxygenases. Curr. Opin. Struct. Biol. *20*, 659–672. https://doi.org/10.1016/j.sbi.2010.08.006.

58. Yasui, T., Hirose, J., Tsutsumi, S., Nakamura, K., Aburatani, H., and Tanaka, S. (2011). Epigenetic regulation of osteoclast differentiation: possible involvement of Jmjd3 in the histone demethylation of Nfatc1. J. Bone Miner. Res. *26*, 2665–2671. https://doi.org/10.1002/jbmr.464.

59. Wang, X., Guo, B., Li, Q., Peng, J., Yang, Z., Wang, A., Li, D., Hou, Z., Lv, K., Kan, G., et al. (2013). miR-214 targets ATF4 to inhibit bone formation. Nat. Med. *19*, 93–100. https://doi.org/10.1038/nm.3026.

60. Shen, L., Hu, P., Zhang, Y., Ji, Z., Shan, X., Ni, L., Ning, N., Wang, J., Tian, H., Shui, G., et al. (2021). Serine metabolism antagonizes antiviral innate immunity by preventing ATP6V0d2-mediated YAP lysosomal degradation. Cell Metab. *33*, 971–987.e6. https://doi.org/10.1016/j.cmet.2021.03.006.

61. Tian, H., Ni, Z., Lam, S.M., Jiang, W., Li, F., Du, J., Wang, Y., and Shui, G. (2022). Precise Metabolomics Reveals a Diversity of Aging-Associated Metabolic Features. Small Methods *6*, e2200130. https://doi.org/10.1002/smtd.202200130.